

Predicting the onset of subglacial drainage channels

K. L. P. Warburton^{1,2}, C. R. Meyer¹, A. N. Sommers¹

¹Thayer School of Engineering, Dartmouth College, Hanover, NH 03755, USA

²Department of Applied Mathematics and Theoretical Physics, University of Cambridge, Cambridge, CB3
0WA, UK

Key Points:

- Feedbacks between subglacial water flow and ice melt determine the rate of incision of drainage channels, depending on their spacing
- We derive a threshold meltwater input above which channels form under glaciers, a function of ice thickness and geothermal flux
- Including lateral heat transport allows continuum models of subglacial hydrology to reproduce Röthlisberger channel behavior

Corresponding author: Kasia Warburton, klpw3@cam.ac.uk

Abstract

The sliding speed of glaciers depends strongly on the water pressure at the ice-sediment interface, which is controlled by the efficiency of water transport through a subglacial hydrological system. The least efficient component of the system consists of ‘distributed’ flow everywhere beneath the ice, whereas the ‘channelised’ drainage through large, thermally eroded conduits is more efficient. To understand the conditions under which the subglacial network channelises, we perform a linear stability analysis of distributed flow, considering competition between thermal erosion and viscous ice collapse. The calculated growth rate gives a stability criterion, describing the minimum subglacial meltwater flux needed for channels to form, but also indicates the tendency to generate infinitely narrow channels in existing models. We demonstrate the need to include lateral heat diffusion when modeling melt incision to resolve channel widths, which allows continuum models to recover R othlisberger channel behavior. We also show that low numerical resolution can suppress channel formation and lead to overestimates of water pressure. Our derived channelization criterion can be used to predict the character of subglacial hydrological systems without recourse to numerical simulations, with practical implications for understanding changes in ice velocity due to changes in surface melt runoff.

Plain Language Summary

Glacier sliding speed depends on the degree of lubrication by water at the bed. During summer months, when there is a lot of water present, heat produced by the water flow can melt large channels into the base of the ice. These channels efficiently drain water out from the bed of the glacier, slowing down the ice flow. We study when and where channels are likely to form by considering whether local increases in water depth grow larger via positive feedback loops, or shrink away. We also look at ways to make simulations less prone to numerical artefacts. We develop a criterion for when channels form and show that our criterion matches the results of numerical simulations, but is much faster to calculate. This can be used to efficiently predict meltwater drainage beneath glaciers, seasonal patterns of ice velocity, and how these will evolve under warming conditions.

1 Introduction

The Greenland Ice Sheet is a major contributor to sea-level rise due to widespread thinning and melting of the ice (Mouginot et al., 2019; Otosaka et al., 2023). Greenland’s glaciers transport ice from the interior of the ice sheet to the ablation zone around the margin. The speed of ice flow is in large part due to sliding at the bed (Rignot & Mouginot, 2012; MacGregor et al., 2016; Maier et al., 2019), the rate of which depends strongly on the effective pressure, defined as the difference between the pressure exerted by the overlying ice and the water pressure (e.g. Schoof, 2005; Helanow et al., 2021; Schoof, 2023; Warburton et al., 2023). Thus, understanding the future of the Greenland Ice Sheet requires an understanding of the way subglacial water pressure evolves in time, over a melt-season and over several decades (Nienow et al., 2017; Aschwanden et al., 2019).

Subglacial hydrological networks span a continuum from inefficient, distributed flow through connected cavities and sediment layers, to channelised, efficient drainage pathways (Schoof, 2010). The transition between distributed and channelised drainage is thought to play a large role in the seasonal patterns of ice sheet velocity across Greenland (Bartholomew et al., 2011; I. J. Hewitt, 2013) and during glacier surges (Benn et al., 2019). For a given volume of surface meltwater passing through the subglacial environment, distributed systems will show higher inland water pressure, lower effective pressure, lower basal friction, and faster flow speeds as compared to the channelised network. Throughout a melt season, basal water pressure generally increases, leading to faster glacier flow (Zwally et

62 al., 2002), until in some cases channelization initiates, the bed drains, and the ice slows
63 (I. J. Hewitt, 2013).

64 Depending on whether the summertime velocities are above or below the winter
65 average, Greenland outlet glaciers can be categorised by type (Moon et al., 2014; Vijay
66 et al., 2021; Poinar, 2023). This categorisation shows some spatial clustering of seasonal
67 patterns, but also reveals that the response of a single glacier can change year-on-year
68 based on the climatic conditions, and neighbouring glaciers can respond quite differently
69 (Tedstone et al., 2015). Models of summertime hydrology often assume that no chan-
70 nels persist through the winter, but some studies show persistent winter channels (Hager
71 et al., 2022; Sommers et al., 2023). Thus a small velocity response could be attributable
72 either to no channelization during the summer or persistent channelization during the
73 winter. Understanding the drivers of current seasonal velocity trends, by predicting when
74 glaciers have channelised subglacial networks, would give better constraints on their fu-
75 ture evolution in a changing climate. Models of future ice sheet evolution generally rely
76 on current estimates of basal slipperiness, which is strongly affected by basal effective
77 pressure and therefore by subglacial channelization (e.g. Morlighem et al., 2010; Seroussi
78 et al., 2013; Shapero et al., 2016).

79 Direct observations of subglacial channels, particularly of their spatial patterning
80 and evolution over a melt-season, are limited (e.g. Andrews et al., 2014; Rada & Schoof,
81 2018). The question of which glaciers have subglacial channels is therefore often left purely
82 to numerical models of the hydrology. However, given the number of such models (c.f.
83 Flowers, 2015), and the differing choices in their modelled processes and parametriza-
84 tions (e.g. Brinkerhoff et al., 2021), the question persists: what balances govern the in-
85 stability of distributed water flow and its tendency to channelise, to what extent are these
86 model-dependent (c.f. de Fleurian et al., 2018), resolution dependent, versus robust phys-
87 ical properties expected of the flow.

88 Walder (1982), in an early study of subglacial water flow, noted the tendency of
89 sheet (distributed) flow to go unstable in ways that rapidly become unphysical, with thicker
90 regions of the sheet able to generate more dissipative heating and melt into the ice above.
91 Beyond this linear instability, nonlinear features such as channels must form (Schoof, 2010).
92 To study this in numerical simulations, many models (c.f. Flowers, 2015; Werder et al.,
93 2013) employ separate equations for the distributed and channelised flow, turning off dis-
94 sipative heating in the distributed regions to prevent this instability from occurring in
95 domains that are designated as sheet flow.

96 In the Subglacial Hydrology And Kinetic, Transient Interactions model (SHAKTI;
97 Sommers et al. (2018)), a single laminar-to-turbulent transitional water-flow model is
98 imposed throughout the domain, and all components of the melt-rate are included ev-
99 erywhere. This allows channel-like features to appear at self-determined locations any-
100 where in the domain. However, despite the ability of the model to produce channel-like
101 features, these features are always one grid point wide, indicating a collapse to the small-
102 est scales, limited only by resolution of the simulation. Further, the spacing, inland ex-
103 tent, and in some cases the appearance of channels itself all depend on the grid size cho-
104 sen, similar to features noted in models of marine ice sheets (Cornford et al., 2016).

105 This tendency towards an infinite narrowing of unstable features, referred to in the
106 context of classical stability analysis as an ‘ultraviolet catastrophe’, is, as described by
107 I. J. Hewitt (2011), indicative of an ill-posed mathematical model for the system, in which
108 the shortest wavelengths are the most unstable, a sign that a process neglected in the
109 model should become important. In his thesis, I. J. Hewitt (2009) derived a maximum
110 growth rate for distributed flow and provided a physical argument that such a break-
111 down ought to occur given the model components. The particular case with no down-
112 stream variation was shown mathematically to break down by Schoof et al. (2012). We
113 also see the ultraviolet catastrophe in the non-convergence of the SHAKTI equations when

114 implemented in adaptive mesh schemes (Felden et al., 2023), in which the channels con-
 115 tinue to narrow towards infinitely small scales. In contrast, a well-posed model should
 116 display wavelength selection, where a perturbation with intermediate wavelength pro-
 117 duces the highest growth rate. Felden et al. (2023) regularised their SUBglacial Hydrol-
 118 ogy MOdel (SUHMO), by introducing a numerically-motivated diffusion-like term and
 119 found this produced convergent channel widths.

120 In this paper, we re-investigate the instability of channel initiation, find the means
 121 to represent channels in a satisfying way within a continuum model, and derive a cri-
 122 terion for rapidly calculating whether or not a drainage system will channelize. We be-
 123 gin by completing the linear stability analysis of distributed flow, reviewing the stabil-
 124 ity criterion of I. J. Hewitt (2009), and confirming the existence of the short-wavelength
 125 blow-up. We also use this to explore the stability of long-wavelength features, and show
 126 how this could lead low-resolution simulations to numerically suppress channel forma-
 127 tion. We then revisit the origin of the melt-rate equation and locate a missing diffusion-
 128 like term, which is similar though not identical to the form posited in Felden et al. (2023).
 129 We find that this term, which we show comes from lateral diffusion of heat, regularises
 130 the stability analysis and allows for wavelength selection, indicating that we have found
 131 a well-posed model of the system. In the final section of the paper, we implement our
 132 new set of equations in an adaptive mesh scheme, and demonstrate that our linear sta-
 133 bility analysis predicts the model results without need for simulation. We show that chan-
 134 nel onset is predicted by our stability criterion, and end by discussing the applicability
 135 of this work to predicting seasonal trends in subglacial hydrology.

136 **2 Analysis of existing models for distributed subglacial flow**

137 **2.1 Model governing equations**

138 In this work, we take as our governing equations those of SHAKTI (Sommers et
 139 al., 2018), but, by design, our results are largely independent of the exact formulation.
 140 The main difference between SHAKTI and other models of subglacial flow is the form
 141 of the power-law relating the flux, water depth, and pressure gradients (see 3.2). That
 142 choice can be changed in the following analysis with only a quantitative, not qualitative
 143 difference to the results.

144 We consider a water-filled space between the ice and bed with effective gap-height
 145 b (figure 1), through which flows a flux of meltwater \mathbf{q} . If the rate at which melt erodes
 146 the water-ice interface over a given area is \dot{m} , then conservation of mass in the fluid layer,
 147 balancing changes in gap height with lateral flow of meltwater and local water sources,
 148 is given by

$$\frac{\partial b}{\partial t} + \nabla \cdot \mathbf{q} = \frac{\dot{m}}{\rho_w} + i_{eb}, \quad (1)$$

149 where ρ_w is the density of water (so \dot{m}/ρ_w is the volume of water produced by basal melt,
 150 per unit area and time) and i_{eb} is the rate at which surface meltwater is delivered to the
 151 bed.

152 Tracking the vertical motion of the ice-water interface due to melting upwards, the
 153 downwards viscous collapse of the overlying ice, and opening by sliding over bumps, we
 154 have

$$\frac{\partial b}{\partial t} = \frac{\dot{m}}{\rho_i} - AN^n b + \frac{(b_r - b)u_b}{l_r}, \quad (2)$$

155 where ρ_i is the density of ice (so \dot{m}/ρ_i is the volume of ice removed by melt, per unit area
 156 and time), u_b is the sliding speed, b_r is the characteristic height of bumps, and l_r the bump
 157 spacing. The collapse term is controlled by A , the viscosity parameter for the ice, with
 158 a power-law exponent n , and N is the effective pressure, the difference between the ice

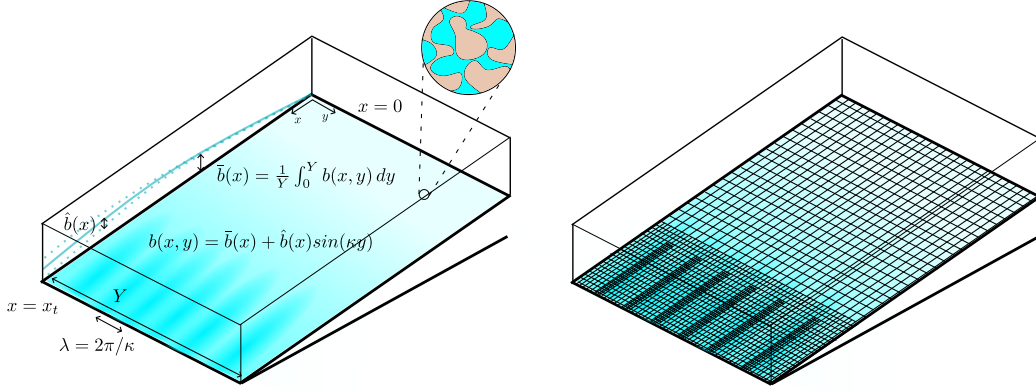


Figure 1. Left, the geometry used in this paper, showing the ice divide at $x = 0$, the terminus as x_t , and an example gap height distribution $b(x, y)$ (color), with width-average $\bar{b}(x)$ and variation of size $\hat{b}(x)$ at a wavelength λ . The spatial structure of pressure head and flux is similarly decomposed into an average plus a periodic perturbation. Away from channels, the effective gap height b represents a local average over flow through connected cavities (inset). Right, a schematic showing mesh refinement in the numerical simulations, with finer meshes in areas of higher spatial variability. Each step in refinement halves the grid size. Both the minimum and maximum levels of refinement can be set manually and we use up to 10 levels (compared to the 3 shown here). Only perturbations where λ is at least twice the minimum grid size can be resolved numerically.

159 overburden and the water pressure,

$$N = p_i - p_w. \quad (3)$$

160 In equation (2), we take the closure lengthscale (average cavity width) as equal to b (Schoof,
 161 2010; Werder et al., 2013; Sommers et al., 2018), but other functions of b have also been
 162 proposed, such as $l_r/(1-b/b_r)$ by Kyrke-Smith et al. (2014). Because opening by slid-
 163 ing over bedrock bumps may be less prominent beneath soft-bedded glaciers without large
 164 protrusions (Zoet & Iverson, 2020; Sommers et al., 2023), we remove it from our exam-
 165 ple calculations, but include it in our formal analysis for comparison with I. J. Hewitt
 166 (2011).

167 We take the flux through the water layer \mathbf{q} , driven by gradients in the pressure head
 168 $h = p_w/\rho_w g + z_b$, to be given by a modified Poiseuille flow,

$$\mathbf{q} = -\frac{b^3 g}{12\nu(1 + \omega Re)} \nabla h, \quad (4)$$

169 where z_b is the bed elevation, ν is the kinematic viscosity of water, $Re = |\mathbf{q}|/\nu = q/\nu$
 170 is the Reynolds number, and ω is a dimensionless parameter describing the frictional re-
 171 sistance in fully developed, turbulent, Darcy-Weisbach flow. The parameter ω therefore
 172 also controls the Reynolds number of transition from laminar to turbulent, at $Re \sim 1/\omega$.
 173 There are other possible formulations of this transition to turbulence (e.g. D. R. Hewitt
 174 et al., 2018), but we take our expression for consistency with prior work on subglacial
 175 hydrology (Sommers et al., 2018; Zimmerman et al., 2004; Hill et al., 2023) and its sim-
 176 ple form.

Symbol	Units	Description
b	m	Effective gap-height
q	$\text{m}^2 \text{s}^{-1}$	Meltwater flux per unit width
\dot{m}	$\text{kg m}^{-2} \text{s}^{-1}$	Melt-rate
i_{eb}	m s^{-1}	Surface meltwater input rate per unit area
ρ_w	kg m^{-3}	Density of water
ρ_i	kg m^{-3}	Density of ice
N	Pa	Effective pressure
p_w	Pa	Water pressure
p_i	Pa	Ice overburden pressure
A	$\text{Pa}^{-n} \text{s}^{-1}$	Viscosity parameter for ice flow
n	-	Ice flow power-law exponent
u_b	m s^{-1}	Ice sliding speed
b_r	m	Characteristic bed bump height
l_r	m	Characteristic bed bump spacing
g	m s^{-2}	Gravitational acceleration
ν	$\text{m}^2 \text{s}^{-1}$	Kinematic viscosity of water
z_b	m	Bed elevation
h	m	Pressure head
ω	-	Transition to turbulence parameter, 0.001
G	W m^{-2}	Geothermal flux
L	J kg^{-1}	Latent heat of fusion of water
τ_b	Pa	Basal shear stress
C	$\text{m}^{-1/2} \text{s}^{1/2}$	Basal friction coefficient (Budd-style sliding)
κ	m^{-1}	Lateral wavenumber
σ	s^{-1}	Growth rate of the perturbation
Σ	-	Dimensionless growth rate constant, 1.0187...
c_p	$\text{J kg}^{-1} \text{K}^{-1}$	Specific heat capacity of water
T	K	Water temperature
k	$\text{W m}^{-1} \text{K}^{-1}$	Thermal conductivity of water
Q	W m^{-3}	Dissipative heating due to water flow
w	m	Channel width
S	m^2	Cross-sectional channel area
Q_c	$\text{m}^3 \text{s}^{-1}$	Melt-water flux through total channel cross-section
M_c	$\text{kg m}^{-1} \text{s}^{-1}$	Total melt on channel walls per unit length
Ω	$\text{m}^2 \text{s}^{-1}$	Meltwater input to channel per unit length
f	-	Shape factor accounting for channel aspect ratio

Table 1. Variables and constants used in this work.

177 Finally, the melt-rate is found by considering a vertical balance of heat fluxes, so
 178 that

$$\dot{m} = \frac{1}{L} (G + |\mathbf{u}_b \cdot \boldsymbol{\tau}_b| - \rho_w g \mathbf{q} \cdot \nabla h), \quad (5)$$

179 where $\dot{m}L$ is the latent heat flux required to melt the ice, G is the geothermal flux, $|\mathbf{u}_b \cdot$
 180 $\boldsymbol{\tau}_b|$ is the frictional heat flux produced by the sliding of the glacier over the bed, and $-\rho_w g \mathbf{q} \cdot$
 181 ∇h is the dissipative heat flux produced by friction in the flow of water itself. We ne-
 182 glect the changes in melting temperature due to pressure variations, which would oth-
 183 erwise appear as a heat source/sink in (5). For the majority of this work, we also assume
 184 all the ice is at melting point, and therefore neglect heat fluxes into the ice. In appendix
 185 B3, we describe how to include temperature gradients within the ice in this framework.

186 We use a Budd-style friction law of the form

$$\tau_b = C^2 N u_b, \quad (6)$$

187 where C is a friction coefficient, taken as uniform in our simulations. The dependence
 188 on the effective pressure N reflects that subglacial hydrology is a strong control on basal
 189 traction, although in this paper we do not account for the feedback of N on the sliding
 190 speed u_b , which we take as known (e.g. from satellite observations). One could also use
 191 a Coulomb sliding law of the form

$$\tau_b = \mu N; \quad (7)$$

192 as both expressions are linear in N the analysis carries through directly with μ in the
 193 place of $C^2 u_b$.

194 2.2 Subglacial hydrology in the absence of channels

195 We first calculate the laterally uniform, constant in time solution to our govern-
 196 ing equations, representing the distributed system before channels form. The growth rate
 197 of the linear perturbations will be determined by this background state.

198 This solution is given by the profiles of gap height, pressure head, and flux

$$b = \bar{b}(x), \quad h = \bar{h}(x), \quad q = \bar{q}(x), \quad (8)$$

199 from $x = 0$, the ice divide, to $x = x_t$, the terminus (figure 1), which solve the govern-
 200 ing equations (1-5) with all time-derivatives and y (lateral) variation ignored,

$$\frac{d\bar{q}}{dx} = \frac{\bar{m}}{\rho_w} + i_{eb}, \quad (9)$$

$$\frac{\bar{m}}{\rho_i} = A \bar{N}^n \bar{b} - \frac{(b_r - \bar{b}) u_b}{l_r}, \quad (10)$$

$$\bar{q} = -\frac{\bar{b}^3 g}{12\nu(1 + \omega \bar{q}/\nu)} \frac{d\bar{h}}{dx}, \quad (11)$$

$$\bar{m} = \frac{1}{L} \left(G + |\mathbf{u}_b \cdot \boldsymbol{\tau}_b| - \rho_w g \bar{q} \frac{d\bar{h}}{dx} \right). \quad (12)$$

201 The ice thickness H (and hence ice overburden pressure $p_i = \rho_i g H$), the bed topog-
 202 raphy z_b , and the surface meltwater input i_{eb} that drive the subglacial hydrology need
 203 to be imposed throughout the modelled domain. For the purposes of the stability anal-
 204 ysis, these drivers are also assumed to be laterally uniform and only functions of distance
 205 from the terminus.

206 The boundary conditions are atmospheric pressure $\bar{p}_w(x_t) = 0$ at the terminus,
 207 and zero meltwater flux $\bar{q}(0) = 0$ at the divide. With one boundary condition at each
 208 end of the domain, we solve these equations using a shooting method: integrating from
 209 the terminus towards the divide, starting with the correct imposed water pressure at the

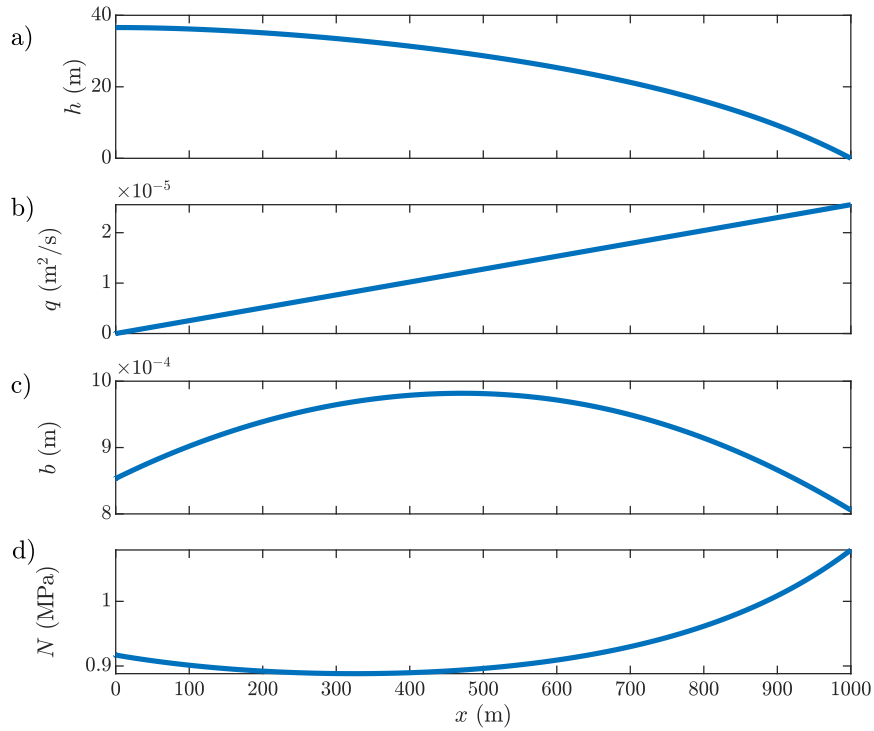


Figure 2. An example of the background solution for a) laterally uniform pressure head \bar{h} , b) water flux \bar{q} , c) gap height \bar{b} , and d) effective pressure \bar{N} solving (9-12) from the ice divide at $x = 0$ to the terminus at 1km, in the case of a constant ice thickness of 120m, distributed meltwater input of 0.8m/year, and a slope of 0.02 (20m drop per km) towards the terminus. Gap opening by sliding is ignored in all simulations.

Grouping	Definition	Interpretation
K	$\frac{\bar{b}^3 g}{12\nu(1+\omega \bar{q} /\nu)}$	Hydraulic transmissivity of distributed flow
Q_b	$\frac{-3\bar{b}^2 g}{12\nu(1+2\omega \bar{q} /\nu)} \frac{d\bar{h}}{dx}$	Speed of gap height advection
Q_h	$\frac{\bar{b}^3 g}{12\nu(1+2\omega \bar{q} /\nu)}$	Transmissivity of head perturbations
U	$\frac{\rho_w g u_b^2 C^2}{L}$	Sensitivity of frictional melt to pressure
M_b	$\frac{36\nu\rho_w \bar{q}^2}{\bar{b}^4 L} \frac{(1+\omega \bar{q} /\nu)^2}{1+2\omega \bar{q} /\nu}$	Sensitivity of melt-rate to gap height
M_h	$\frac{\rho_w g \bar{q}}{L} \frac{2+3\omega \bar{q} /\nu}{1+2\omega \bar{q} /\nu}$	Sensitivity of melt-rate to pressure gradients

Table 2. Definitions of the functions of the background state used to streamline the stability analysis, and their physical interpretations.

terminus and a guess of the outflow flux $\bar{q}(x_t)$, then use a root-finding algorithm to refine the outflow until there is no flux at the ice divide, $\bar{q}(0) = 0$.

An example solution is shown in figure 2 for constant ice thickness, basal slope, and surface meltwater input (values of parameters given in caption). In this example, the subglacial water flux \bar{q} increases nearly linearly towards the terminus, fed by the constant input of meltwater from the surface and low dissipative heating. This leads to a high pressure head \bar{h} in the interior that decreases rapidly towards the terminus. The gap height \bar{b} initially increases to accommodate the additional meltwater, but drops towards the terminus due to the increased rate of viscous ice collapse as the effective pressure \bar{N} increases.

2.3 Initial linear growth rate of channels

With these background conditions established, we now introduce small periodic perturbations on top of the background state and calculate whether any wavelengths lead to perturbations that are expected to grow (leading to eventual channelization) or if instead disturbances decay back towards the distributed system found above. We find it convenient to define several parameter groupings, based on the background state, which the behavior of these perturbations, given in Table 2.

Each possible cross-flow wavelength $\lambda = 2\pi/\kappa$ is associated with a growth rate $\sigma(\kappa)$ and an along-flow structure $\hat{b}(x)$, $\hat{h}(x)$ and $\hat{q}(x)$, which describe how the perturbations evolve between the terminus and the ice divide (figure 1). The overall perturbed gap height, pressure head, and flux are given by

$$b = \bar{b}(x) + \hat{b}(x)e^{i\kappa y + \sigma t}, \quad (13)$$

$$h = \bar{h}(x) + \hat{h}(x)e^{i\kappa y + \sigma t}, \quad (14)$$

$$q = \bar{q}(x) + \hat{q}(x)e^{i\kappa y + \sigma t}. \quad (15)$$

These expressions are substituted into the governing equations (1-5), until we obtain a pair of differential equations for $\hat{h}(x)$ and $\hat{b}(x)$, for which $\sigma(\kappa)$ is the eigenvalue allowing all boundary conditions to be simultaneously met. For full details of this procedure, see Appendix B1; the main conceptual steps are given here.

We find that the perturbation to changes in the motion of the ice-water interface (2) are given by

$$\left(\sigma - \frac{M_b}{\rho_i} + A\bar{N}^n + \frac{u_b}{l_r} \right) \hat{b} = \left(An\bar{N}^{n-1}\rho_w g \bar{b} - \frac{U}{\rho_i} \right) \hat{h} - \frac{M_h}{\rho_i} \frac{\partial \hat{h}}{\partial x}. \quad (16)$$

238 This describes how changes in gap height depend on to changes in collapse rate (through
 239 changes in pressure and in gap height) and changes in melt-rate (through changes in ther-
 240 mal dissipation from changes in pressure gradients and gap height).

241 Note that if there were no perturbation to the pressure head, i.e. $\hat{h}(x) = 0$, the
 242 growth rate would be given by a local, wavelength-independent competition between the
 243 tendency of larger gaps promote melt via accommodating faster, more dissipative flow,
 244 and their more rapid collapse, which we denote by

$$\sigma_0 = \frac{M_b}{\rho_i} - A\bar{N}^n - \frac{u_b}{l_r}. \quad (17)$$

245 The shape of $\sigma_0(x)$ for the example of figure 2 is shown in figure 3a, and in general is
 246 negative (suppressing channelization) close to the ice divide, where M_b is small, but in-
 247 creases towards the terminus. Turning off dissipative heating in the distributed system
 248 corresponds setting M_b zero, which completely removes the possibility of instability or
 249 channel initiation from regions of initially distributed flow.

250 Meanwhile, the perturbation to conservation of mass (1) simplifies to

$$\sigma\hat{b} = -\frac{\partial}{\partial x} \left(Q_b\hat{b} - Q_h\frac{\partial\hat{h}}{\partial x} \right) - K\kappa^2\hat{h} + \frac{M_b}{\rho_w}\hat{b} - \frac{U}{\rho_w}\hat{h} - \frac{M_h}{\rho_w}\frac{\partial\hat{h}}{\partial x}. \quad (18)$$

251 This equation describes how the larger, longer wavelength perturbations tend to be sta-
 252 bilised due to the large gradients in pressure head required to sustain flow into them (compare
 253 to the similar stabilisation by mass conservation noted in Brinkerhoff et al., 2016).

254 Solving for \hat{h} , \hat{b} , and σ as a function of κ is in general only possible numerically given
 255 the complex structure of the background state. To do so, for each value of κ , we guess
 256 a value of σ , begin with very small \hat{h} and \hat{b} close to the ice divide, then integrate the equa-
 257 tions forwards towards the terminus to find $\hat{h}(x_t)$. We then iteratively update the value
 258 of σ until we find a value producing $\hat{h}(x_t) = 0$, pressure at the terminus matching onto
 259 atmospheric pressure. These numerically calculated values of $\sigma(\kappa)$ for the example back-
 260 ground state of figure 2 are shown in figure 3b.

261 However, we can make further progress and find an explicit expression for the growth
 262 rate in the limit of large κ (short wavelengths). In particular, this is the relevant limit
 263 for examining the short-wavelength blow-up. Further, figure 3b shows that the large κ
 264 limit turns out to provide a good match to the numerically derived values throughout
 265 the range of unstable wavenumbers. Again, details of the calculation can be found in Ap-
 266 pendix B1, but the key insight is that the perturbations are confined to a region close
 267 to the terminus, where $Q_b(x)$, $K(x)$, and $M_h(x)$ are approximately constant, while $\sigma-$
 268 $\sigma_0(x)$ is small and taken to be a linear function of x . If there are strong gradients in ice
 269 overburden pressure, $\sigma_0(x)$ can have a maximum inland of the terminus, requiring a slight
 270 modification to the short wavelength analysis, discussed in Appendix B4.

271 Under these assumptions, we can explicitly calculate the growth rate associated with
 272 each wavelength, along with the corresponding shape of the pressure head and gap height
 273 perturbations. We find that \hat{b} is localised close to the terminus, given by a re-scaled Airy
 274 function of the first kind,

$$\hat{b} = Ai \left(\left(\frac{\rho_i K \kappa^2 (\partial\sigma_0/\partial x)}{Q_b M_h} \right)^{1/3} (x_t - x) - \Sigma \right) \quad (19)$$

275 while the corresponding perturbed pressure head is proportional to the derivative of \hat{b} ,
 276 and peaks slightly inland of the terminus,

$$\hat{h} = \left(\frac{Q_b}{K\kappa^2} \right)^{2/3} \left(\frac{\rho_i (\partial\sigma_0/\partial x)}{M_h} \right)^{1/3} Ai' \left(\left(\frac{\rho_i K \kappa^2 (\partial\sigma_0/\partial x)}{Q_b M_h} \right)^{1/3} (x_t - x) - \Sigma \right). \quad (20)$$

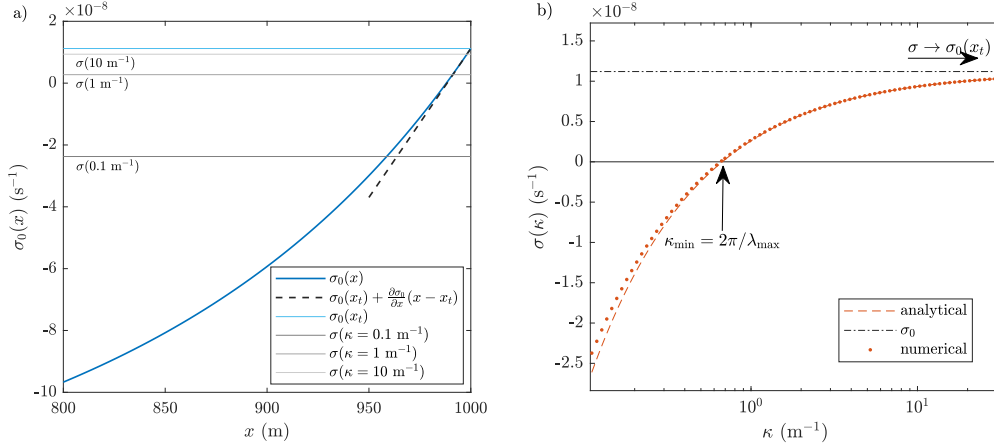


Figure 3. a) The local balance of melt versus collapse, $\sigma_0(x)$, increases towards the terminus and is eventually is greater than the growth rate for any given wavenumber. The linearisation close to the terminus is plotted to show the validity of the analytic approach. b) Growth rates of perturbations to the background state shown in figure 2, dots calculated as numerical eigenvalues to eqs. (16,18) and dashed line calculated analytically per eq. (21). The agreement between the two curves improves as $\kappa \rightarrow \infty$, the limit for which the analytic result is derived. Wavelengths longer than λ_{\max} from eq. (48) are stable, and the shortest wavelengths (largest κ) are the most unstable, tending towards a growth rate of σ_0 per eq. (17).

277 Here $\Sigma = 1.0187\dots$ is the smallest value at which the Airy function has zero deriva-
 278 tive, chosen so that the pressure boundary condition at the terminus is met. Plots of these
 279 functions, and their correspondence to numerical simulations of the full system of equa-
 280 tions, are shown in figure 7e-f. The growth rate σ of perturbation at a wavelength $\lambda =$
 281 $2\pi/\kappa$ is given by

$$\sigma = \sigma_0(x_t) - \Sigma \left(\frac{\partial \sigma_0}{\partial x} \right)^{2/3} \left(\frac{Q_b M_h}{\rho_i K \kappa^2} \right)^{1/3}, \quad (21)$$

282 shown in figure 3b.

283 2.4 Interpretation of the linear growth rate

284 Beyond its agreement with the numerically determined eigenvalues, we note two
 285 important properties of equation (21), plotted in figure 3b. Firstly, the growth rate in-
 286 creases as $\kappa \rightarrow \infty$, indicating an unphysical breakdown of the governing equations since
 287 the shortest wavelengths are the most unstable. This demonstrates why the channels that
 288 develop when these equations are simulated numerically always narrow until they are the
 289 size of the finest scale resolved. Secondly, as $\kappa \rightarrow \infty$, $\sigma \rightarrow \sigma_0(x_t)$ from below, so
 290 $\sigma_0(x_t)$ is an upper bound on the growth rate of all scales of perturbations. Thus, the sign
 291 of $\sigma_0(x_t)$ determines the overall stability of the system. Substituting the form of M_b from
 292 table 2 into expression (17) for σ_0 , and using (10) and (12) to express the melt-rate in
 293 terms of the heat sources, we have instability if

$$\frac{2 + \omega|\bar{q}|/\nu}{1 + 2\omega|\bar{q}|/\nu} \rho_w g \bar{q} \left| \frac{d\bar{h}}{dx} \right| > G + |\mathbf{u}_b \cdot \boldsymbol{\tau}_b| + \rho_i L \frac{b_r u_b}{l_r} \quad (22)$$

294 at the terminus. We can interpret the terms on the right hand side as the types of heat-
 295 ing that allow the distributed system to persist, while the terms on the left are the heat-
 296 ing that occurs primarily in rapid channel flow. Thus, channels develop when the melt-
 297 rate enhancement provided by channelised flow is enough to open up areas of significantly

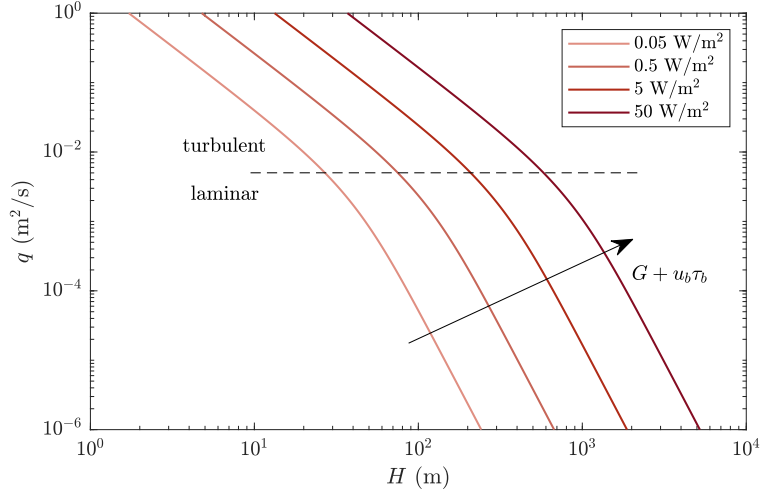


Figure 4. Minimum flux through the terminus (approximately the total volumetric meltwater input, plus melt due to basal heat flux, over the catchment area, divided by the terminus width) needed for channels to initiate, as a function of the ice thickness at the terminus, according to equation (24), for a range of basal heat fluxes $G + u_b \tau_b$. The break-in-slope corresponds to the laminar-turbulent transition in the hydrology model. Opening by sliding is ignored in this plot, but could be included using equation (24).

298 higher gap heights, altering the permeability of the subglacial network and feeding back
 299 into reduced water pressure and higher collapse rate away from the channels.

300 With $\omega = 0$, i.e. assuming laminar flow everywhere in the distributed system, equa-
 301 tion (22) agrees with the critical discharge condition of I. J. Hewitt (2011).

$$2\rho_w g \bar{q} \left| \frac{d\bar{h}}{dx} \right| > G + |\mathbf{u}_b \cdot \boldsymbol{\tau}_b| + \rho_i L \frac{b_r u_b}{l_r}, \quad (23)$$

302 which came from assuming *a priori* that $\hat{h} = 0$, which we have shown is indeed con-
 303 sistent with the short wavelength limit. Also, since the x scale over which perturbations
 304 decay, given by (B15), looks like $\kappa^{-2/3}$, and shrinks more slowly than the wavelength in
 305 the y direction, $2\pi\kappa^{-1}$, this analysis is consistent with a simpler instability calculation
 306 in Schoof (2010) that neglects gradients in x , again highlighting that the behavior is generic
 307 despite slightly different formulations of the system.

308 A more tractable reframing of (22) comes from using (10) and (11) to rewrite the
 309 instability criterion in terms of \bar{N} rather than $d\bar{h}/dx$. Since the criterion is evaluated at
 310 the terminus, where $\bar{N} = p_i = \rho_i g H$ is just the ice overburden pressure, while \bar{q} can
 311 be estimated from inputs and basal melt over the catchment area, this formulation is eas-
 312 ily to evaluate for glaciers. We find instability if

$$\frac{192}{27} \frac{\left(1 + \frac{\omega|\bar{q}|}{2\nu}\right)^4 \left(1 + \frac{2\omega|\bar{q}|}{\nu}\right)}{\left(1 + \frac{\omega|\bar{q}|}{\nu}\right)^2} \rho_w \nu \bar{q}^2 \left[\rho_i L \left(A(\rho_i g H)^n + \frac{u_b}{l_r} \right) \right]^3 > \left(G + |\mathbf{u}_b \cdot \boldsymbol{\tau}_b| + \rho_i L \frac{b_r u_b}{l_r} \right)^4, \quad (24)$$

313 which can be read as a frictional-heat-flux-dependent lower bound on $\bar{q}^2 H^9$ at the ter-
 314 minus, above which channels start to form (figure 4). The instability initiates when ei-
 315 ther high effective pressures close down the distributed system, or high basal fluxes pro-
 316 mote channelised melt, compared to the terms on the right that promote opening of the

317 distributed system. We demonstrate the power of this stability criterion in predicting
 318 the behavior of full numerical simulations of subglacial hydrology in section 5.1. How-
 319 ever, the same stability analysis also predicts a numerical breakdown at short wavelengths,
 320 which we turn our attention to next.

321 **3 Inclusion of heat transport for improved modeling of channels**

322 The breakdown of existing models of distributed subglacial flow at short wavelengths
 323 has been previously noted, and numerically overcome in many ways, from turning off dis-
 324 sipative heating in the distributed system (Werder et al., 2013), imposing a minimum
 325 channel width (effectively Sommers et al., 2018), or adding a diffusive term to the gap
 326 dynamics (Felden et al., 2023). These approaches seek to minimise the impact of this
 327 unphysical behavior; instead, we consider the assumptions that introduce the unphys-
 328 icality in the first place, providing a more consistent way to regularise the model. We
 329 will show, similar to the analysis of Walder (1982), that by considering in more detail
 330 the structure of the thermal profile in the water layer, a laterally diffusive term appears
 331 (this time in the melt-rate) that provides a physical mechanism for regularisation.

332 To revisit the derivation of the melt-rate in equation (5), we start from the heat
 333 equation

$$\rho_w c_p \left(\frac{\partial T}{\partial t} + \mathbf{u} \cdot \nabla T \right) - k \nabla^2 T = Q, \quad (25)$$

334 where c_p is the specific heat capacity, k is the thermal conductivity of water and Q is
 335 the dissipative heating from the water flow. Since the depth of the water layer is small,
 336 we would expect vertical diffusion of temperature to be the dominant mechanism for heat
 337 transport. We therefore neglect the advective terms on the left hand side of (25) and ig-
 338 nore the horizontal derivatives in ∇^2 , resulting in

$$-k \frac{d^2 T}{dz^2} = Q. \quad (26)$$

339 Depth-integrating this equation, applying the geothermal flux and ice-bed frictional heat-
 340 ing at the base of the water layer, we find that the heat flux into the ice at the top of
 341 the water layer is

$$-k \left. \frac{dT}{dz} \right|_{z=b} = G + |\mathbf{u}_b \cdot \boldsymbol{\tau}_b| + \int_0^b Q dz. \quad (27)$$

342 Equating this heat flux with the latent heat flux required to melt the ice, $\dot{m}L$, gets us
 343 back to equation (5) for the melt-rate. However, note that the assumption that verti-
 344 cal gradients in temperature dominate over lateral gradients breaks down when the hori-
 345 zontal lengthscale becomes similar to the vertical scale, which happens as the wavelengths
 346 become small. Reintroducing lateral heat transport is therefore a plausible way to reg-
 347 ularise the short-wavelength behavior.

348 **3.1 Heat transport away from channels**

349 From the above discussion, we see that the missing process in our governing equa-
 350 tions is a transport of heat from areas of high heat production (i.e. the dissipative chan-
 351 nelerized flow) towards colder areas - that is, our modeled channels were infinitely narrow
 352 because they could only melt upwards, not into their sidewalls. We therefore need to in-
 353 troduce a term to describe this lateral heat transport, and its impact on the location of
 354 melt relative to the location of thermal dissipation.

355 We begin by calculating the heat flux into the ice, which comes from an integral
 356 of the heat equation in the water layer. However, rather than integrating the simpler (26),
 357 which ignores lateral temperature diffusion, we depth-integrate the full steady heat equa-

358 tion (25) and obtain

$$-k \left(\nabla_H \cdot \int_0^b \nabla_H T dz - \nabla_H b \cdot \nabla_H|_{z=b} T \right) = G + k \frac{\partial T}{\partial z} \Big|_{z=b} + |\mathbf{u}_b \cdot \boldsymbol{\tau}_b| + \int_0^b Q dz. \quad (28)$$

359 where ∇_H denotes horizontal gradients, and we have pulled one horizontal derivative
360 outside the integral and generated a boundary term from the spatially varying b .

361 To then calculate the melt-rate, we balance the latent heat of melting with the heat
362 flux into the ice from the water. Since we are now considering how the melting of sloping
363 interfaces can act to widen channels, we draw a distinction between \dot{m} , the rate at
364 which the interface appears to move upwards (which we will use in the expression for the
365 motion of the interface, equation (2)), and \dot{M} , the rate at which the interface moves in
366 the direction normal to itself due to melting, where the direction of the normal is

$$\hat{\mathbf{n}} = \frac{1}{\sqrt{1 + (\nabla_H b)^2}} \left(-\frac{\partial b}{\partial x}, -\frac{\partial b}{\partial y}, 1 \right). \quad (29)$$

367 These two rates are geometrically linked via the slope of the interface, $\dot{m} = \sqrt{1 + (\nabla_H b)^2} \dot{M}$.
368 Physically, the heat flux into the interface balances the melting into the interface, so

$$\dot{M}L = -\frac{k}{\sqrt{1 + (\nabla_H b)^2}} \left(\frac{\partial T}{\partial z} - \nabla_H b \cdot \nabla_H T \right). \quad (30)$$

369 Now, we work to put all of our expressions in terms of b and \dot{m} only, rather than
370 depending on the temperature structure inside the water layer. Since all the ice is assumed
371 to be at the melting temperature, $T(b) = T_m$. Thus if there are horizontal variations
372 in T close to the ice interface, they can be directly related to changes in the distance
373 to that interface, and so by applying the chain rule for differentiation we find

$$\nabla_H|_{z=b} T = -\frac{\partial T}{\partial z} \nabla_H b. \quad (31)$$

374 We can insert (31) into (30) to write the vertical and horizontal temperature fluxes in
375 terms of the melt-rate and geometry,

$$k \frac{\partial T}{\partial z} = -\frac{\dot{m}L}{1 + |\nabla_H b|^2}, \quad k \nabla_H|_{z=b} T = \frac{\dot{m}L}{1 + |\nabla_H b|^2} \nabla_H b. \quad (32)$$

376 Inserting these expressions into (28), we obtain

$$\dot{m}L - \nabla_H \cdot \int_0^b k \nabla_H T dz = G + |\mathbf{u}_b \cdot \boldsymbol{\tau}_b| + \int_0^b Q dz. \quad (33)$$

377 The new term represents the lateral transport of heat via diffusion, so that melt-rate is
378 not only dependent on the local dissipation rate, but also on the heating in neighbouring
379 areas. In fact, examining equation (33), we can still interpret this as a balance of heat
380 fluxes, now including the divergence of horizontal sensible heat fluxes.

381 We finally make the approximation that horizontal temperature gradients (which
382 in general depend on the detailed structure of the temperature field) are well-approximated
383 by their value close to the ice-water interface (known), and so use (32) for the lateral heat
384 flux everywhere inside the integral. We thus obtain

$$\dot{m} = \frac{1}{L} (G + |\mathbf{u}_b \cdot \boldsymbol{\tau}_b| - \rho_w g \mathbf{q} \cdot \nabla h) + \nabla_H \cdot \left(\frac{b \dot{m} \nabla_H b}{1 + |\nabla_H b|^2} \right), \quad (34)$$

$$= \dot{m}_0 + \nabla_H \cdot \left(\frac{b \dot{m} \nabla_H b}{1 + |\nabla_H b|^2} \right) \quad (35)$$

385 This is the same as our original melt-rate equation (5), but with a new, non-local, melt-
 386 diffusion term that allows areas of high local heat fluxes to also cause melting in their
 387 surroundings. We still only need to simulate the gap height, pressure head, and melt-
 388 rate, so (34) can be used with equations (1-4) to simulate subglacial hydrology exactly
 389 as before, although now \dot{m} appears on both sides of equation (34). This structure requires
 390 a slightly altered numerical solution approach, described in section 4.

391 The term is similar in structure to the gap-height diffusion term introduced in Felden
 392 et al. (2023), with two key differences. Firstly, the full melt-rate is included in the dif-
 393 fusivity here, rather than, as in SUHMO,

$$D = \frac{b}{\rho_i L} (-\rho_w g \mathbf{q} \cdot \nabla h), \quad (36)$$

394 only the dissipative contribution to the melt-rate. This distinction is less important in
 395 regions with high basal water flux, but more significant where geothermal flux dominates.
 396 Secondly, as a structural difference, it appears directly in the expression for the melt-
 397 rate, versus in Felden et al. (2023), where the gap-height diffusion term is only used to
 398 regularize one of the evolution equations for b , with

$$\frac{\partial b}{\partial t} = \frac{\dot{m}_0}{\rho_i} + \beta u_b - AN^n b + \nabla \cdot (D \nabla b). \quad (37)$$

399 However, the precedent set by their work gives confidence that a diffusional term of this
 400 nature is sufficient to dampen the short-wavelength blow-up, as we show in the next sec-
 401 tion. The linearised analysis will also confirm that the melt-diffusion term in (34) reas-
 402 suringly agrees with the form found from the full linearised analysis (B24).

403 3.2 Recovery of R othlisberger channel behavior

404 When adding lateral heat diffusion to the SHAKTI equations, the width of the chan-
 405 nels is no longer grid-size dependent but converges to a finite width (figure A1). In this
 406 section we show that the evolution of these self-selecting features is comparable to the
 407 behavior of R othlisberger channels in models for which separate equations are imposed
 408 for the distributed and channelised portions of the domain. Throughout this section we
 409 use x to denote the along-channel, and y to denote the cross-channel coordinate.

410 Integrating mass conservation (1) across a channel of width w , we get

$$\frac{\partial S}{\partial t} + \frac{\partial Q_c}{\partial x} = -\frac{\partial q_y}{\partial y} + \frac{\dot{M}_c}{\rho_w} + i_{eb} w, \quad (38)$$

411 where S is the cross-sectional area of the channel, Q_c is the total flux through the chan-
 412 nel, \dot{M}_c is the total melt on the channel wall, $\Omega = -\partial q_y / \partial y$ is the input of meltwater
 413 from the distributed system, and $i_{eb} w$ is the input of surface meltwater landing directly
 414 in the channel, which we can neglect, to get

$$\frac{\partial S}{\partial t} + \frac{\partial Q_c}{\partial x} = \Omega + \frac{\dot{M}_c}{\rho_w}, \quad (39)$$

415 along with the integral of gap height evolution (2) which gives

$$\frac{\partial S}{\partial t} = \frac{\dot{M}_c}{\rho_i} - AN^n S. \quad (40)$$

416 Integrating the melt equation (34) across the width of the channel, and neglect-
 417 ing heat diffusion in the along-channel direction, we have

$$\dot{M}_c = \frac{1}{L} \left((G + |\mathbf{u}_b \cdot \boldsymbol{\tau}_b|) w - \rho_w g Q_c \frac{\partial h}{\partial x} \right) + \frac{b \dot{m}}{1 + (\partial b / \partial y)^2} \frac{\partial b}{\partial y}, \quad (41)$$

418 where the final lateral heat flux term is evaluated at the sides of the channel. If we again
 419 neglect the background terms (proportional to w) as small compared to the dissipative
 420 melting, and drop the lateral heat flux since b and \dot{m} are small at the very edges of the
 421 channel, we arrive at

$$\dot{M}_c = \frac{Q_c}{L} \frac{\partial h}{\partial x}. \quad (42)$$

422 To find the flow law giving Q_c , we need to link the width of the channel to its height.
 423 To find such a scaling relationship, we combine equations (34) and (2), ignore opening
 424 by sliding (anticipating that $b > b_r$), and take the limit of long, quasi-steady channels
 425 by neglecting t - and x - derivatives,

$$0 = \dot{m}_0 - \rho_i A N^n b + \frac{\partial}{\partial y} \left(\frac{\dot{m} b}{1 + (\partial b / \partial y)^2} \frac{\partial b}{\partial y} \right). \quad (43)$$

426 This is a differential equation for $b(y)$, where \dot{m}_0 also depends on b through \mathbf{q} . We do
 427 not attempt to solve (43) directly for the shape $b(y)$. Instead, we argue that for large
 428 melt-rates, the shape of the channel is set by a balance between dissipation near the centre
 429 of the channel, and lateral diffusion of heat causing melt into the channel sidewalls.
 430 A balance between these terms can only hold if $b \sim y$, and so the width of channels must
 431 be comparable to their height. Thus, integrating (4) in the limit of high Re , we have

$$Q_c = \frac{(g|\nabla h|)^{1/2}}{(12\omega)^{1/2}} \int_{-w/2}^{w/2} b(y)^{3/2} dy = \frac{(g|\nabla h|)^{1/2}}{(12f\omega)^{1/2}} S^{5/4} \quad (44)$$

432 where f is a shape factor relating the integral of $b^{3/2}$ across the width of the channel to
 433 $S^{5/4}$, since both scale like $b^{5/2}$. The shape factor will depend on the exact shape of the
 434 channel (e.g. for exactly semi-circular channels, $f \approx 1.44$).

435 Equations (39, 40, 42, 44) are exactly the conservation equations expected for R othlisberger
 436 channels (Werder et al., 2013), and therefore the introduction of lateral heat transport
 437 to SHAKTI via the new diffusion term is expected to reproduce the expected channelised
 438 behavior.

439 3.3 Validation of model regularisation

440 We now show, via linear stability analysis of the governing equations with lateral
 441 heat transport included, that the shortest wavelengths in the system have been stabilised,
 442 and therefore we would no longer expect to see infinite narrowing of simulated channels.

443 The details of the calculation can be found in Appendix B2. We solve for the per-
 444 turbations in the temperature profile through the water layer, $T = \bar{T}(z) + \hat{T}e^{i\kappa y}$, and
 445 in the dissipative heating $Q = \bar{Q} + \hat{Q}e^{i\kappa y}$, associated with a gap height perturbation
 446 $\hat{b}e^{i\kappa y}$. We then calculate the perturbation to the melt-rate accounting for lateral heat
 447 transport.

448 The introduction of lateral diffusion of heat modifies the overall growth rate found
 449 in (21) to

$$\sigma = \sigma_0(x_t) - \frac{\bar{m}\bar{b}}{\rho_i} \kappa^2 - \Sigma \left(\frac{\partial \sigma_0}{\partial x} \right)^{2/3} \left(\frac{Q_b M_h}{\rho_i K \kappa^2} \right)^{1/3}, \quad (45)$$

450 which, as shown in figure 5, is stable at both the largest and smallest wavenumbers.

451 Importantly, we now have a maximum growth rate at a finite value of κ , since σ
 452 decreases quadratically as κ gets large. This indicates that we have regularised the short
 453 wavelength singularity. The most unstable wavenumber is at approximately

$$\kappa = \left(\frac{\Sigma \rho_i}{3\bar{m}\bar{b}} \right)^{3/8} \left(\frac{\partial \sigma_0}{\partial x} \right)^{1/4} \left(\frac{Q_b M_h}{\rho_i K} \right)^{1/8}. \quad (46)$$

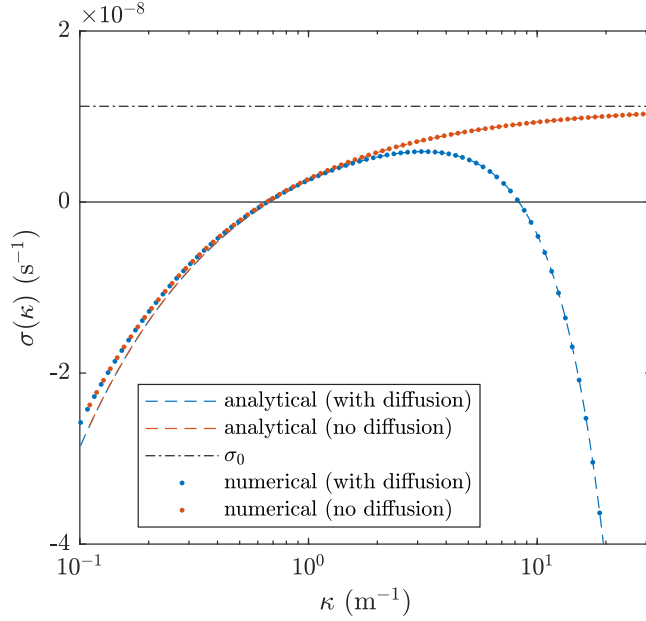


Figure 5. Impact of including lateral temperature diffusion on the growth rates of perturbations. In red, the original model, as in figure 3b. In blue, the modified growth rates including melt-diffusion: dots are numerical eigenvalues of (B25,B26) and dashed line shows the analytic growth rate (45). The shortest wavelengths are now stabilised: there is a most unstable wavenumber given by (46), with growth rate given by (47).

454 While this wavelength is small (comparable to the thickness of the water layer), the chan-
 455 nels produced by the modified system of equations should no longer be infinitely nar-
 456 row. The maximum growth rate is slightly reduced by the diffusive effects to

$$\sigma = \sigma_0(x_t) - 4 \left(\frac{\bar{m}\bar{b}}{\rho_i} \right)^{1/4} \left(\frac{\Sigma}{3} \right)^{3/4} \left(\frac{\partial\sigma_0}{\partial x} \right)^{1/2} \left(\frac{Q_b M_h}{\rho_i K} \right)^{1/4}, \quad (47)$$

457 as can be seen in figure 5, the maximum growth rate is somewhat less than σ_0 . However,
 458 the stability criterion (24) based only on $\sigma_0(x_t)$ still holds to good approximation (e.g.
 459 figure 6a).

460 We have demonstrated that our improved set of governing equations produce wave-
 461 length selection, and thus should not be prone to the previous unphysical breakdown at
 462 small scales. We next perform numerical simulations of these equations to demonstrate
 463 both the validity of our analysis and to illustrate the power of the linearised analysis for
 464 predicting the behavior of subglacial hydrology without resorting to full numerical sim-
 465 ulation.

466 4 Simulation results

467 We implemented the SHAKTI governing equations, with the additional melt-diffusion
 468 term, in the adaptive-mesh PDE solver Basilisk (Popinet, 2013–2024) using the inbuilt
 469 Poisson solver to calculate the pressure head and flux, and an explicit fixed time-step
 470 forward Euler method to update the gap height. The subglacial geometry and melt-rate
 471 are only updated during the explicit time-step, and kept at this value during the follow-
 472 ing Poisson solve routine. For ease of implementation, we used the value of melt-rate from
 473 the previous timestep to calculate the lateral heat transport term appearing in (34). The

474 mesh adaptation and interpolation are handled by the `adapt` routine of Basilisk. The
 475 adaptive mesh allowed us to locally reach much higher resolutions than possible in the
 476 original ISSM implementation of SHAKTI (Sommers et al., 2018).

477 We perform the majority of our simulations in the same idealised test geometry as
 478 Sommers et al. (2018), a 1km square domain with uniform ice thickness and slope of 0.02
 479 towards the outflow boundary, at which we impose atmospheric pressure, while the other
 480 three sides of the domain are no-flux boundaries. We focus on a test case that is close
 481 to the stability boundary, 120m-thick ice with distributed meltwater input of 0.8m per
 482 year throughout the domain (matching the scenario presented in figures 2, 3 and 5 of this
 483 paper). The simulations are initiated with a gap height in the range 0.9-1 mm, independ-
 484 ently selected from a uniform random distribution for each mesh cell. The simulations
 485 rapidly converge to something close to the laterally-uniform base state, with small de-
 486 viations away from this localised near the terminus.

487 4.1 Channel development

488 We ran simulations varying meltwater inputs between 0.4 and 0.8m per year and
 489 ice thicknesses between 110m and 140m. Figure 6a records whether or not channels de-
 490 veloped after a year of simulation time. The outcome is well-predicted by our stability
 491 criterion (24).

492 For the case of 0.8m per year input, 120m-thick ice, the deviation of gap height away
 493 from the laterally-averaged value is shown in figure 7. The gap height in the interior con-
 494 verges to the distributed state, while the perturbations close to the margins grow, be-
 495 fore merging to form channels. These channels then propagate back into the interior of
 496 the domain. A video of the full timeline of channel evolution is available in the supple-
 497 ment.

498 4.2 Minimum resolution requirement

499 For coupled ice-hydrology models, we would ideally simulate the subglacial hydrology
 500 at the same resolution as that of ice flow, i.e. on a grid at the kilometre scale, but
 501 this is not plausible with our model, as the resolution of numerical simulations can dra-
 502 matically impact the behavior of the simulated water flow. Since long wavelengths are
 503 always stable (figures 3b and 5) due to the scale of pressure gradients they induce, sim-
 504 ulations on a coarse grid may appear stable even in a regime where instability is expected.
 505 The maximum unstable wavelength,

$$\lambda_{\max} = \frac{2\pi}{\Sigma^{3/2}} \left(\frac{\rho_i K}{Q_b M_h} \right)^{1/2} \frac{\sigma_0(x_t)^{3/2}}{\partial\sigma_0/\partial x}, \quad (48)$$

506 found by setting the growth rate in (21) to 0, controls the scale above which any distur-
 507 bances decay away. If the smallest scales resolved by the simulation are larger than this
 508 wavelength, the numerical simulation will not produce instability, since the only drivers
 509 of channelization would occur on smaller scales than can be resolved. Thus, we find chan-
 510 nels can be suppressed numerically in situations where a physical balance would predict
 511 instability. This results in the persistence of an inefficient drainage system, leading to
 512 an overestimate of basal water pressure (figure 8). In a coupled simulation, this numer-
 513 ical artefact would therefore lead to an overestimate of sliding velocities throughout this
 514 region.

515 To illustrate this effect, we simulated the same idealised test case across a range
 516 of maximum grid resolutions. We deliberately chose a configuration that was only just
 517 unstable, leading to a fairly small value of $\lambda_{\max} = 9.52$ m according to (48). Basilisk
 518 requires the number of gridpoints to be a power of 2, so for our 1km domain we tested
 519 meshes from $1000/2^6 = 15.625$ m to $1000/2^{10} = 0.977$ m. Channelization was sup-
 520 pressed by the 15.6m and 7.81m meshes, but occurs with the 3.91m mesh and smaller,

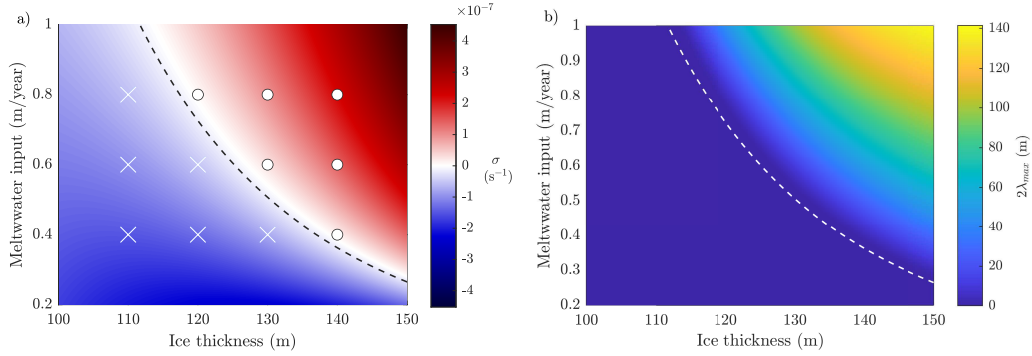


Figure 6. a) effect of varying meltwater input and ice thickness on three metrics of channelization. Dashed line gives the approximate stability criterion (24), where we use total meltwater input and geothermal melting only to estimate of flux at the terminus. Color shows σ , the maximum growth rate predicted by (47), using a 1D calculation of \bar{q} that includes dissipative melt at the bed. Outcomes from the full numerical simulations are superimposed - crosses indicate no channels, circles indicate channels developed. When the maximum predicted growth rate is positive, channelization is indeed observed. The boundary predicted by (24) lies just inside the stable regime according to (47) due to the impact of melt-diffusion, which is not considered in (24). b) predicted minimum mesh side length needed to resolve instability, equal to $2\lambda_{\max}$, from (48). Regions without instability are shown as 0. Channels are most vulnerable to numerical suppression close to the margin of stability, when the required mesh size gets small.

521 since at this mesh size and below at least two grid points fit within an unstable wave-
 522 length and an unstable oscillation can be simulated (figure 8).

523 Although simulating a full glacier at a resolution below 4m is currently unreason-
 524 able, figure 6b shows that the minimum resolution required to capture the instability grows
 525 rapidly, to a scale of hundreds of metres, as we move away from the stability boundary.
 526 Thus, caution is only needed close to the onset of channel formation. Even a relatively
 527 low-resolution model will predict channelization if the system is unstable enough.

528 However, figure 8 also demonstrates that even when channel formation is captured,
 529 the inland extent and spacing of the channels remain grid-dependent until the width of
 530 the channels is well-resolved. Without melt-diffusion, channels remain one grid-cell wide
 531 (c.f. Felden et al., 2023) and the channel spacing never converges. Including the melt-
 532 diffusion term allows for finite width channels and for the channel distribution to con-
 533 verge, but requires resolutions higher than the width of channels (c.f. Appendix A1).

534 5 Discussion

535 5.1 Channel initiation is a predictable linear process

536 Both the growth rate (45) and the stability criterion (24) successfully predict whether
 537 or not channels develop in numerical simulations, over a range of surface meltwater in-
 538 puts and ice thicknesses (figure 6a). Channelization occurs if the flow-rate within the chan-
 539 nels is high, especially if strong creep-closure elsewhere prevents water from leaving through
 540 the distributed system. Thus, we see channels form when the rate of meltwater input
 541 is large (high dissipative heating and local melt keeps the channels open) and when the
 542 ice sheet is thicker (ice overburden pressure promotes closure and tamps down on the
 543 distributed system). The stability criterion (24) depends only on the glacier geometry

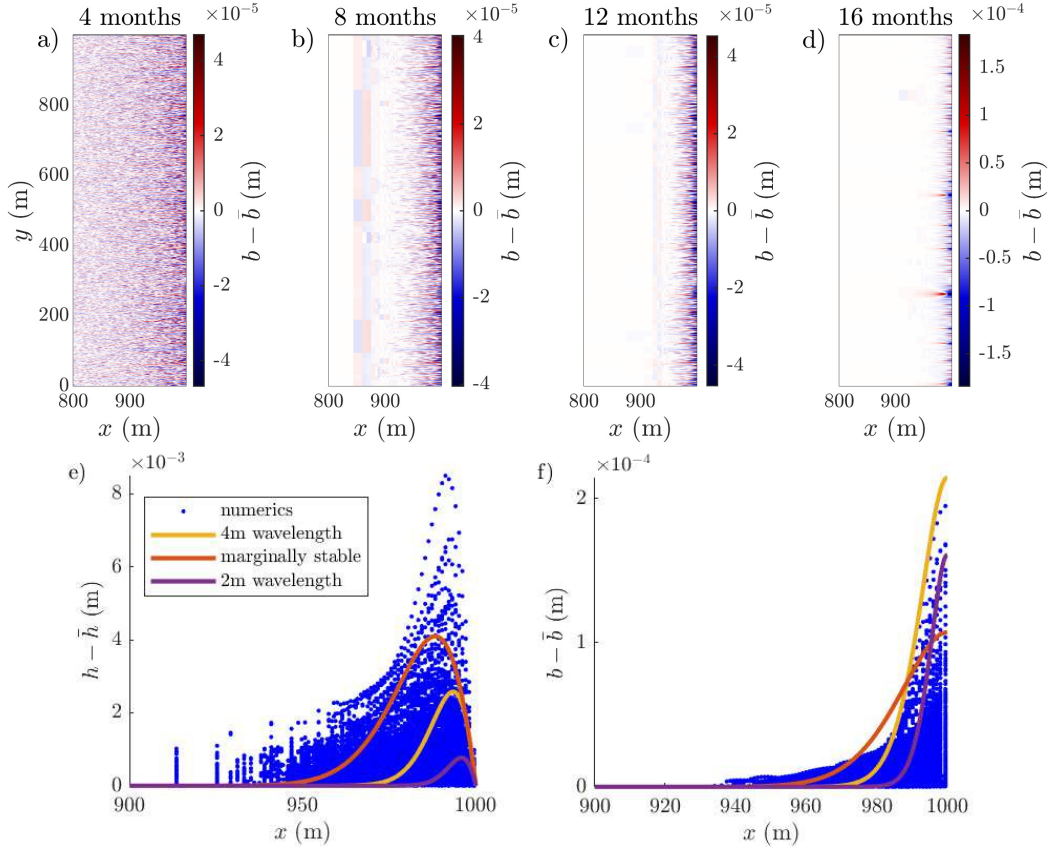


Figure 7. a-d), evolution of the deviation in gap height away from the width-averaged value. Initially, the deviation is due to the random noise introduced everywhere in the domain. The perturbations with the largest lengthscales are stable and thus decay away, leaving only the narrow fluctuations close to the terminus. These small-scale perturbations are unstable and grow into channels propagating back into the interior of the domain. The larger scale blocks seen ~ 200 m from the terminus are artefacts from mesh adaptation. e-f), comparison between the numerical deviation from average pressure head (e) and gap height (f) at 12 months, and the Airy eigenfunctions for a range of unstable wavelengths. The relative size of \hat{h} and \hat{b} is set by (20), and thus the agreement in both amplitude and shape give additional confidence in the analytic results. The persistence into the interior and the somewhat larger $h - \bar{h}$ than predicted can be attributed to longer wavelength, stable modes that are still decaying away.

544 and estimates of net surface meltwater input within the catchment area. As it can be
 545 quickly evaluated, it provides a quick estimate of the character of subglacial flow to compare
 546 with spatio-temporal patterns of glacier velocity, without running a full numerical
 547 simulation.

548 Beyond the stability criterion, the structure of the variations in gap height and water
 549 pressure are also well-predicted by the stability analysis. In the unstable cases, the
 550 initial perturbations first develop close to the margin of the ice sheet, at a wavelength
 551 comparable to the most unstable mode (46). The along-flow structure of the growing gap-
 552 height and water-pressure perturbations match the shapes predicted by the Airy eigen-
 553 functions (figure 7), with large variability close to the margins, decaying inland. This
 554 suggests that channels are more likely close to termini (in agreement with observations

555 and simulations; Werder et al., 2013; Poinar et al., 2019) as they initiate in this near-
 556 terminus region of large pressure perturbations and then propagate inland.

557 A potential implementation would be to apply the stability criterion over a range
 558 of catchment areas across Greenland, under both summer and winter conditions. From
 559 this one could assess if basal melt leads to persistent wintertime channels, if distributed
 560 drainage networks remain through summer, or if channels are expected to develop dur-
 561 ing the melt season. Relating these predicted behaviors to the amplitude of the seasonal
 562 velocity response would then provide a strong test for our model. In the opposite direc-
 563 tion, we could assess how much meltwater input is required to change the seasonal flow
 564 of a glacier, or if current wintertime channels minimise the potential impact of any fu-
 565 ture seasonal melt on accelerating ice velocity. This is particularly relevant not only for
 566 Greenland, but also for mountain glaciers that experience seasonal melt, and for the fu-
 567 ture of the Antarctic ice sheet as the area warms.

568 **5.2 Strong non-linearity of channel propagation**

569 As the perturbations develop and propagate inland, they become non-linear fea-
 570 tures: large, distinct channels surrounded by almost fully-drained areas of distributed
 571 flow, far from a small perturbation in sheet depth. These features evolve according to
 572 the equations for Röthlisberger channels (see 3.2). The interactions between neighbour-
 573 ing channels involve complex, long-range competition for the meltwater delivered from
 574 the surface. Channels that lose out on meltwater suddenly collapse, with winning chan-
 575 nels growing rapidly into the vacated space (video in supplementary). As such, the dy-
 576 namics that govern the evolution of channel spacing cannot be explained using linear sta-
 577 bility analysis. The most unstable wavelength, despite its importance to the early-time
 578 patterns of channels, is not visible in the final configuration of the subglacial hydrology.

579 Predicting the number of channels in a catchment area, their average spacing, and
 580 net effect on the subglacial water pressure remains challenging. From an analysis of the
 581 pressure distribution around a single, non-evolving channel, I. J. Hewitt (2011) suggested
 582 that the spacing of channels should be similar to their length. Our final configurations
 583 show a somewhat smaller spacing (e.g. in figure 8, around one third of their length). Over-
 584 all, being able to predict the evolution of average properties of the subglacial system (such
 585 as channel spacing and effective pressure) without simulating individual channels is a
 586 goal for reduced modeling. Numerical simulations can provide an important inspiration
 587 for the development of such models, but are vulnerable to producing numerical artefacts,
 588 an example of which we discuss below.

589 **5.3 Relevance to more realistic scenarios**

590 The configuration we study here is idealised in two main ways: the simple, laterally-
 591 uniform geometry, and the meltwater input that is kept constant in time. In the sim-
 592 ulations shown in figure 8, the meltwater input is kept constant over a timescale of years
 593 to allow the channels to fully develop to a steady configuration, a poor representation
 594 of seasonal melt for Greenland and mountain glaciers. In part, this is due to our focus
 595 on conditions close to marginal stability, where the growth rates of instabilities are small.
 596 In more unstable configurations, the growth rate (figure 6) is orders of magnitude larger,
 597 so channels develop on a timescale of weeks. This illustrates that it is not only the sign
 598 of the maximum growth rate (47), but also its magnitude, that controls whether large
 599 channels develop during a melt season. To explain the the seasonal patterns of subglacial
 600 hydrology, we would need to look at the total time-integrated growth rate with varying
 601 meltwater input, to assess if and when the first channel-sized features appear. We leave
 602 this for future work.

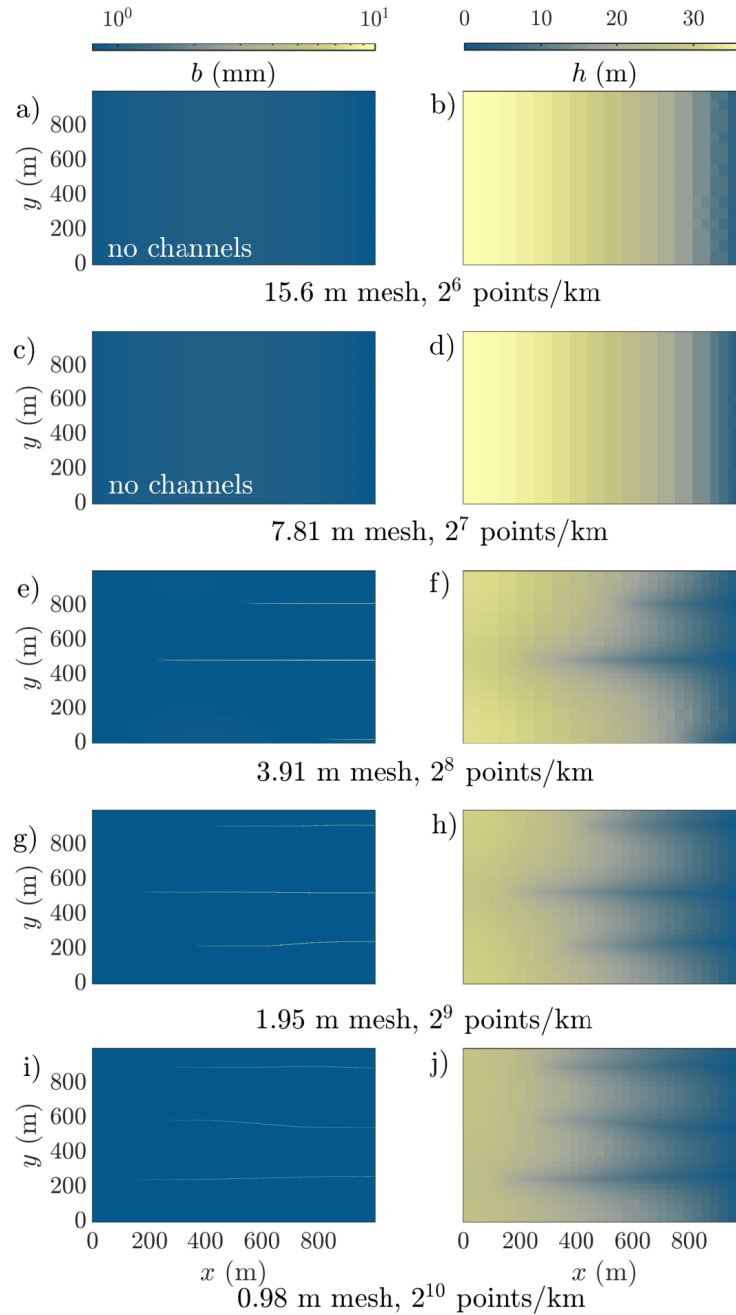


Figure 8. The impact of varying resolution on the state of the simulated subglacial hydrology after 10 years of simulation time. Minimum mesh size halves with each plot from top to bottom. Left panels show gap height b (in mm, log colorscale), and right the corresponding pressure head h (in m). The channels are regions of lower water pressure compared to the surrounding regions, pulling meltwater from their surroundings and funnelling it towards the margin (right hand side of domain). Large meshes suppress channelization and result in higher inland water pressures. The final channel spacing, unrelated to the linear initiation, emerges as neighbouring channels compete and migrate inland (video in supplementary).

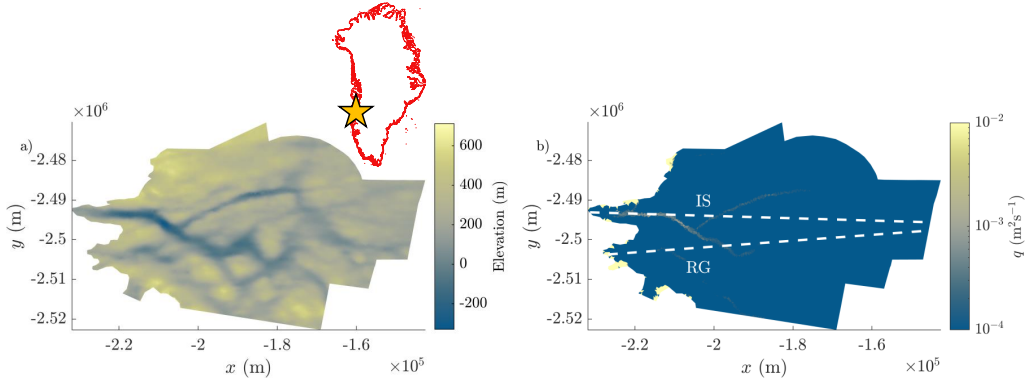


Figure 9. a) Topography beneath Russell Glacier (RG) and Isunnguata Sermia (IS). The inset shows the location in southwest Greenland. b) Subglacial water flux beneath RG and IS under winter conditions, as simulated in SHAKTI. A channel develops beneath IS following the lows in basal topography (Morlighem et al., 2017). Dashed lines indicate the profiles of topography and ice thickness used for the stability calculations.

603 Our simplified geometry allows us to perform stability analysis using a background
 604 state that is uniform across the width of the terminus, leading to the appearance of self-
 605 selecting, randomly distributed perturbations across the domain. The basal topography
 606 of real glaciers and ice streams is heterogeneous at a range of scales, guiding both the
 607 location of channel initiation and the pathways in the final channel configuration (e.g.
 608 Hiester et al., 2016; de Fleurian et al., 2018; Dow, 2022). However, our analysis still high-
 609 lights the fundamental competition between channelising melt and viscous ice collapse
 610 that governs the question of channelization. Thus, we may still be able to predict which
 611 glaciers are likely to feature an efficient subglacial network based on a representative as-
 612 sessment of criterion (24) at the glacier terminus.

613 As a demonstration, we ran SHAKTI in the ISSM framework on a domain includ-
 614 ing Russell Glacier (RG) and Isunnguata Sermia (IS) in Southwest Greenland under win-
 615 ter (no surface meltwater input) conditions (per Sommers et al., 2023), using geometry
 616 from BedMachine v4 (Morlighem et al., 2017) and velocities from MEaSURES (Joughin
 617 et al., 2018). As shown in figure 9, a channel forms under IS but not under RG. We com-
 618 pare this to the maximum growth rate of instabilities based on 1D profiles down the mid-
 619 lines of each glacier (dashed lines on figure 9). We find a positive growth rate of $1.33 \times$
 620 10^{-7}s^{-1} at IS, consistent with channel development. At RG, which has thinner ice at
 621 the terminus, the maximum growth rate is $-6.79 \times 10^{-8}\text{s}^{-1}$. The negative value indi-
 622 cates that distributed flow is indeed expected during the winter. These results indicate
 623 that linear stability analysis can provide a characterisation of subglacial hydrology even
 624 in more complex domains.

625 6 Conclusions

626 To better understand both the channelization of subglacial hydrology and numer-
 627 ical models thereof, we have performed a full linear stability analysis of distributed sub-
 628 glacial flow, finding a stability criterion and the growth rates of different scales of per-
 629 turbations.

630 We confirmed the existence of a short-wavelength blow-up in the original model
 631 of distributed water flow, under which channels always narrow unphysically to the small-

est scale of the simulation. We demonstrated that consistent, convergent simulated behavior can be achieved through the re-introduction of lateral temperature diffusion to the model, and have derived a melt-rate diffusion term to parameterise this effect, allowing for its smooth integration into existing modeling frameworks. We also showed that long wavelength perturbations are always stabilised, due to the large pressure gradients they induce, and thus derived a minimum resolution requirement (48) below which numerical models are unable to resolve the onset of channelization.

Importantly, we have demonstrated that channels initiate when the enhanced melt due to heat produced by flow inside a channel overwhelms the balance between geothermal and viscous ice collapse that controls the distributed flow network. This criterion (24) provides a rapid estimate of when and where an efficient subglacial system is expected to form, and thus opens a path for understanding the seasonal trends of glacier velocity and their possible changes in a warming climate, without recourse to a full numerical model. Application of this efficient calculation holds high potential for interpreting and projecting future changes in ice velocity caused by changes in water flow beneath glaciers and ice sheets.

Appendix A Validation of Basilisk implementation

A1 Comparison to SUHMO: single channel from a moulin

We implemented the same channelising test case as in SUHMO (Felden et al., 2023), a 64 m domain with a bedslope of 0.02 (20m drop per km) and a slab of ice of constant 500 m thickness. A moulin delivering $30\text{m}^3\text{s}^{-1}$ of water is located 16 m from the margin with a Gaussian profile in space. The moulin input is gradually increased in time, from 0 at time $t = 0\text{s}$ to the maximum value after about a month, and the simulation proceeds until steady state is reached.

Similarly to the SUHMO results, the channel converges towards a fixed height and width with increasing numerical resolution (figure A1). We produce a wider, less tall channel than in SUHMO (6 m vs 3 m wide, 0.9m vs 1.5m high) due to the higher diffusivity that includes the geothermal flux, promoting enhanced widening rates in the channels.

A2 Comparison to ISSM

We simulated the 120m ice, 0.6m/year melt configuration in both the ISSM Version 4.21 and Basilisk implementations of SHAKTI. This case is predicted not to channelise (figure 6), providing a test of the Poisson solver, as both should converge towards the same laterally uniform state. Indeed, we found the same distributions of pressure head and gap height in both implementations (figure A3).

We then tested 130m thick ice with 0.8m/year of meltwater, which as predicted results in channels in both the ISSM and Basilisk implementations (figure A4). Both simulations developed two large channels and one small channel. The location of the channels differs between simulations, which is to be expected from the randomly seeded initial perturbation.

These two experiments give confidence that our Basilisk implementation of the SHAKTI governing equations is correct.

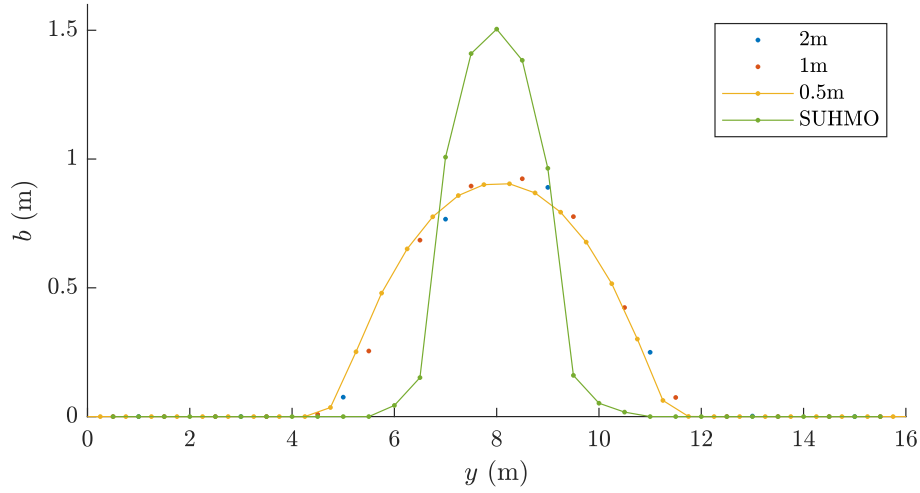


Figure A1. Gap height b at a transect 10m inland of the margin, when a large moulin is located 16m inland of the margin. We see convergence in channel width and height with increasing resolution. The same example in SUHMO produces a taller, narrower channel, as expected.

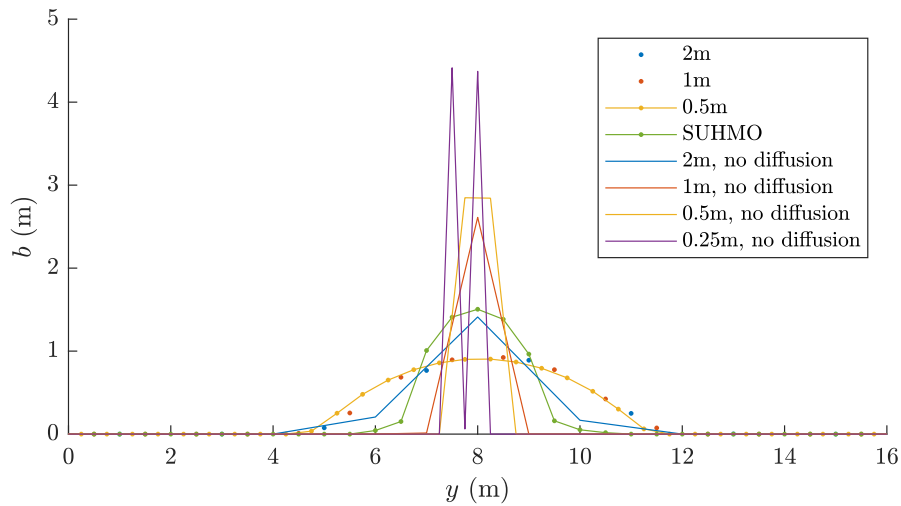


Figure A2. The same moulin configuration as in figure A1, with the addition of the results of the original SHAKTI equation (without melt-diffusion). The original model results do not converge with increasing mesh resolution.

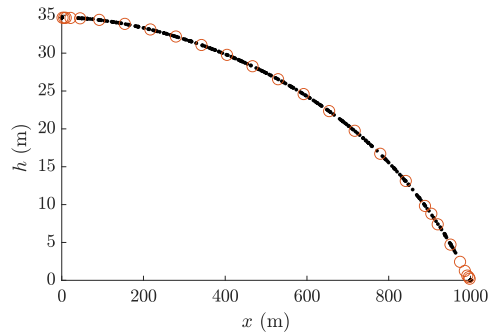


Figure A3. Pressure head from the ISSM (black dots) and Basilisk (red circles) implementations of SHAKTI show complete agreement throughout the domain in the distributed case (with 0.6m/year of meltwater input, 120 m thick ice, after 10 years of simulation time.)

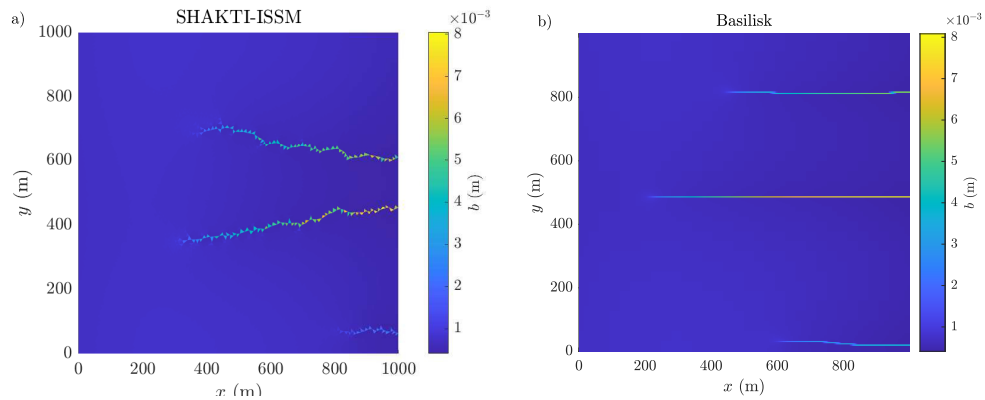


Figure A4. Channels that developed in a 1km square domain, with 0.8m/year of meltwater input, 130 m thick ice, after 10 years of simulation time. a) With the ISSM implementation of SHAKTI, using an average mesh side length of 5 m (minimum 3.84m), b) with the Basilisk implementation of SHAKTI, and a minimum mesh size of 3.91 m.

Appendix B Details of the linear stability analysis

B1 Original system of equations

We start from the governing equations (1-5), and insert the perturbed gap height, pressure head, and flux expressions

$$b = \bar{b}(x) + \hat{b}(x)e^{i\kappa y + \sigma t}, \quad (\text{B1})$$

$$h = \bar{h}(x) + \hat{h}(x)e^{i\kappa y + \sigma t}, \quad (\text{B2})$$

$$\mathbf{q} = \bar{\mathbf{q}}(x) + \hat{\mathbf{q}}(x)e^{i\kappa y + \sigma t}. \quad (\text{B3})$$

We work in a laterally infinite and uniform domain, so all values of κ are possible. Since there is no y or t dependence in the background state, each mode of perturbation has the same values of κ and σ across all variables.

Substituting these expressions into the equation for the flux (4), and retaining only the terms linear in the perturbations, we find that the perturbed flux can be expressed in terms of the background state and the gap and pressure head perturbations as

$$\hat{\mathbf{q}} = -\frac{\bar{b}^3 g}{12\nu(1 + \omega|\bar{q}|/\nu)} \left[\frac{1 + \omega|\bar{q}|/\nu}{1 + 2\omega|\bar{q}|/\nu} \left(\frac{3\hat{b}}{\bar{b}} \frac{d\bar{h}}{dx} + \frac{\partial\hat{h}}{\partial x} \right) \hat{\mathbf{x}} + i\kappa\hat{h}\hat{\mathbf{y}} \right] \quad (\text{B4})$$

and the perturbation to the divergence in flux is therefore

$$\widehat{\nabla \cdot \mathbf{q}} = \left(\frac{\partial}{\partial x} \left[\frac{-\bar{b}^3 g}{12\nu(1 + 2\omega|\bar{q}|/\nu)} \left(\frac{3\hat{b}}{\bar{b}} \frac{d\bar{h}}{dx} + \frac{\partial\hat{h}}{\partial x} \right) \right] + \frac{\bar{b}^3 g \kappa^2}{12\nu(1 + \omega|\bar{q}|/\nu)} \hat{h} \right). \quad (\text{B5})$$

For convenience in the following analysis, we give names to these functions of the base state (table 2), and write

$$\widehat{\nabla \cdot \mathbf{q}} = \frac{\partial}{\partial x} \left(Q_b \hat{b} - Q_h \frac{\partial\hat{h}}{\partial x} \right) + K \kappa^2 \hat{h}. \quad (\text{B6})$$

The functions $Q_b(x)$, $Q_h(x)$, and $K(x)$ are always positive, and describe how easily variations in pressure and gap height are transported in different regions of the distributed system.

Substituting the expression for the flux into the melt-rate (5), we find that melt-rate perturbations can also be expressed in terms of pressure head and gap height,

$$\hat{m} = \frac{\rho_w g}{L} \left(-u_b^2 C^2 \hat{h} - \frac{1 + \omega|\bar{q}|/\nu}{1 + 2\omega|\bar{q}|/\nu} \frac{3}{\bar{q}} \frac{d\bar{h}}{dx} \hat{b} - \frac{2 + 3\omega|\bar{q}|/\nu}{1 + 2\omega|\bar{q}|/\nu} \frac{\partial\hat{h}}{\partial x} \right). \quad (\text{B7})$$

Again, we give names to these functions of the base state (table 2), so

$$\hat{m} = -U(x)\hat{h} + M_b(x)\hat{b} - M_h \frac{\partial\hat{h}}{\partial x}. \quad (\text{B8})$$

Here, $U(x)$ describes the impact of pressure variations on friction at the glacier bed, $M_b(x)$ describes how sensitive the melt-rate is to changes in gap height, and $M_h(x)$ describes how changes in pressure gradients impact the melt-rate through changes in flow rate. Again, all these functions are defined so as to be positive quantities (the sensitivity of melt-rate to the different variables). Turning off dissipative heating in the distributed system corresponds to a case where M_h and M_b are both zero, which we shall see immediately removes the possibility of instability or channel initiation in these regions.

Inserting these results into the motion of the ice-water interface (2), we obtain a first equation linking changes in water pressure to the growth rate of the gap height perturbation,

$$\left(\sigma - \frac{M_b}{\rho_i} + A\bar{N}^n + \frac{u_b}{l_r} \right) \hat{b} = \left(A n \bar{N}^{n-1} \rho_w g \bar{b} - \frac{U}{\rho_i} \right) \hat{h} - \frac{M_h}{\rho_i} \frac{\partial\hat{h}}{\partial x}. \quad (\text{B9})$$

705 In the limit where pressure perturbations played no role and $\hat{h} = 0$, the growth rate
706 would be given by

$$\sigma_0 = \frac{M_b}{\rho_i} - A\bar{N}^n - \frac{u_b}{l_r}. \quad (\text{B10})$$

707 Meanwhile, the perturbation to conservation of mass (1) simplifies to

$$\sigma\hat{b} = -\frac{\partial}{\partial x} \left(Q_b\hat{b} - Q_h\frac{\partial\hat{h}}{\partial x} \right) - K\kappa^2\hat{h} + \frac{M_b}{\rho_w}\hat{b} - \frac{U}{\rho_w}\hat{h} - \frac{M_h}{\rho_w}\frac{\partial\hat{h}}{\partial x}. \quad (\text{B11})$$

708 This equation describes how the larger, longer wavelength perturbations tend to be sta-
709 bilised due to the large gradients in pressure head required to sustain flow into them (compare
710 to the similar stabilisation by mass conservation noted in Brinkerhoff et al., 2016)

711 Together, the pair of differential equations for \hat{h} and \hat{b} (B9, B11) at a particular
712 value of κ has the structure of an eigenfunction problem, where the growth rate $\sigma(\kappa)$ is
713 the eigenvalue, i.e. the only value of σ that allows all the boundary conditions to be si-
714 multaneously met. The boundary conditions are $\hat{h}(0) = 0$ (no pressure variations at
715 the terminus, as the outflow pressure is the same everywhere); the decay of \hat{h} and \hat{b} to-
716 wards the ice divide (inspecting the structure of the differential equations, this turns out
717 to be a single condition); and finally since both equations are linear and we can multi-
718 ply both $\hat{b}(x)$ and $\hat{h}(x)$ by any constant value without affecting the structure of the so-
719 lution, we impose $\hat{b}(0) = 1$ for convenience.

720 In the limit of large κ (short wavelengths), we can make further analytic progress.
721 We anticipate that variations in the pressure head will be small, $\hat{h} \ll 1$, so that the $\kappa^2\hat{h}$
722 term in (B11) remains balanced. We therefore also expect $\sigma - \sigma_0 \ll 1$ as we will be
723 close to the $\hat{h} = 0$ solution to (B9), and so find that $\partial\hat{h}/\partial x \ll \hat{b}$. Finally, in order to
724 keep all the boundary conditions we must preserve the \hat{b} -derivative in (B11), which im-
725 plies that $x \ll 1$. Under these assumptions, equation (B11) becomes

$$\hat{h} = -\frac{1}{K\kappa^2} \frac{\partial(Q_b\hat{b})}{\partial x}, \quad (\text{B12})$$

726 which, substituted into (B9), yields

$$\frac{\partial^2(Q_b\hat{b})}{\partial x^2} = \frac{\rho_i K \kappa^2}{M_h} (\sigma - \sigma_0) \hat{b}, \quad (\text{B13})$$

727 a single second order differential equation for \hat{b} .

728 With $x \ll 1$, our perturbations are confined to a boundary layer close to the ter-
729 minus, so we can approximate $Q_b(x)$, $K(x)$, and $M_h(x)$ as constants, and their termi-
730 nus values. Unless otherwise stated, going forwards we will take these variables to refer
731 to their values at the terminus. However, since $\sigma - \sigma_0(x)$ is small and changes sign
732 within the boundary layer (figure 3a), we retain the next term in its expansion, which
733 is linear in x . Under these approximations, (B13) becomes

$$\frac{\partial^2\hat{b}}{\partial x^2} = \frac{\rho_i K \kappa^2}{Q_b M_h} \left(\sigma(\kappa) - \sigma_0(x_t) + \frac{\partial\sigma_0}{\partial x}(x_t - x) \right) \hat{b}. \quad (\text{B14})$$

734 Recognising this differential equation structure as Airy's equation, we see that in the limit
735 of small wavelengths, the structure of the gap height perturbation $\hat{b}(x)$ must be a rescaled
736 Airy function. By scaling the growth rate $\sigma - \sigma_0(x_t)$ and the inland distance x using

$$\sigma_0(x_t) - \sigma = \Sigma \left(\frac{\partial\sigma_0}{\partial x} \right)^{2/3} \left(\frac{Q_b M_h}{\rho_i K \kappa^2} \right)^{1/3}, \quad x_t - x = \left(\frac{Q_b M_h}{\rho_i K \kappa^2 (\partial\sigma_0/\partial x)} \right)^{1/3} X, \quad (\text{B15})$$

737 (B14) simplifies to

$$\frac{\partial^2\hat{b}}{\partial X^2} = (X - \Sigma) \hat{b}, \quad (\text{B16})$$

738 exactly Airy's equation with a shifted coordinate system, with the rescaled growth rate
 739 Σ setting the shift. Since we require our perturbations decay inland, \hat{b} must be an Airy
 740 function of the first kind, i.e. $\hat{b} = Ai(X - \Sigma)$, and substituting this into (B12),

$$\hat{h} = \left(\frac{Q_b}{K\kappa^2} \right)^{2/3} \left(\frac{\rho_i(\partial\sigma_0/\partial x)}{M_h} \right)^{1/3} Ai'(X - \Sigma). \quad (\text{B17})$$

741 Thus, to match on to atmospheric pressure, Σ is chosen so that $\hat{h}(0) = Ai'(-\Sigma) = 0$,
 742 so $\Sigma = 1.0187\dots$ and

$$\sigma = \sigma_0(x_i) - 1.0187 \left(\frac{\partial\sigma_0}{\partial x} \right)^{2/3} \left(\frac{Q_b M_h}{\rho_i K \kappa^2} \right)^{1/3}. \quad (\text{B18})$$

743 While there are infinitely many other possible values of z such that $Ai'(-z) = 0$, they
 744 are increasingly large, and so associated with smaller growth rates; the associated per-
 745 turbations are always more stable and less relevant to the dynamics of the system.

746 B2 Inclusion of lateral heat transport

747 As before, since the gap height is small, we expect strong gradients in z , and since
 748 we wish to capture the short-wavelength behavior, we also retain gradients in y . In this
 749 limit, the linearised form of the heat equation (25) reduces to diffusion of temperature
 750 with a heat source,

$$-k \left(\frac{\partial^2 \hat{T}}{\partial z^2} - \kappa^2 \hat{T} \right) = \hat{Q}. \quad (\text{B19})$$

751 The boundary conditions remain a geothermal flux at the base, and that the ice-water
 752 interface is at melting temperature, which in terms of the perturbed quantities become

$$-k \left. \frac{\partial \hat{T}}{\partial z} \right|_{z=0} = 0, \quad \left. \frac{\partial \bar{T}}{\partial z} \right|_{z=\bar{b}} \hat{b} + \hat{T}(\bar{b}) = \hat{T}(\bar{b}) - \frac{\bar{m}L}{k} \hat{b} = 0. \quad (\text{B20})$$

753 We solve the linearised diffusion equation (B19) with these boundary conditions, and find
 754 that the profile of the corresponding temperature change is

$$\hat{T} = \left[\left(\frac{\bar{m}L}{k} \hat{b} - \frac{\hat{Q}}{k\kappa^2} \right) \frac{\cosh(\kappa z)}{\cosh(\kappa \bar{b})} + \frac{\hat{Q}}{k\kappa^2} \right], \quad (\text{B21})$$

755 and in particular the additional heat flux into the ice is

$$-k \left. \frac{\partial \hat{T}}{\partial z} \right|_{z=\bar{b}} - k \left. \frac{\partial^2 \bar{T}}{\partial z^2} \right|_{z=\bar{b}} \hat{b} = \frac{\tanh(\kappa \bar{b})}{\kappa} \hat{Q} + (\bar{Q} - \kappa \tanh(\kappa \bar{b}) \bar{m}L) \hat{b}, \quad (\text{B22})$$

756 which, equating to the latent heat of melting $\dot{m}L$, corresponds to a melt-rate perturba-
 757 tion

$$\hat{m} = \frac{1}{L} \left(\frac{\tanh(\kappa \bar{b})}{\kappa} \hat{Q} + (\bar{Q} - \kappa \tanh(\kappa \bar{b}) \bar{m}L) \hat{b} \right). \quad (\text{B23})$$

758 To simplify this further, we consider the case where the background gap height is small,
 759 so $\tanh(\kappa \bar{b}) \approx \kappa \bar{b}$. Then (B23) becomes

$$\hat{m} = \frac{1}{L} \left(\hat{Q} \bar{b} + \bar{Q} \hat{b} \right) - \kappa^2 \bar{b} \bar{m} \hat{b} = \hat{m}_0 - \kappa^2 \bar{b} \bar{m} \hat{b}, \quad (\text{B24})$$

760 where \hat{m}_0 is the perturbation in melt-rate when ignoring lateral heat transport, previ-
 761 ously found in equation (B8). We see that including lateral diffusion of heat has intro-
 762 duced a new term proportional to $-\kappa^2 \hat{b}$, which has the structure of a diffusion of gap height
 763 away from narrowly channelising regions. Equation (B24) is structurally similar to equa-
 764 tion (14) of Walder (1982), although the rest of that analysis proceeded to neglect the

765 diffusion term, arguing it was too small to impact the water layer dynamics, which is true
 766 except when κ becomes very large.

767 We now demonstrate that our lateral heat diffusion term regularises the linear sta-
 768 bility analysis. With the new melt-diffusion term modifying the melt-rate perturbation
 769 from (B8) into (B24), the equations (B9) and (B11) for the structure of the pressure head
 770 \hat{h} and gap height \hat{b} perturbations are slightly modified to

$$\left(\sigma - \frac{M_b}{\rho_i} + A\bar{N}^n + \frac{u_b}{l_r} + \frac{\bar{m}\bar{b}}{\rho_i}\kappa^2\right)\hat{b} = \left(A\bar{n}\bar{N}^{n-1}\rho_w g\bar{b} - \frac{U}{\rho_i}\right)\hat{h} - \frac{M_h}{\rho_i}\frac{\partial\hat{h}}{\partial x} + \frac{\partial}{\partial x}\left(\frac{\bar{m}\bar{b}}{\rho_i}\frac{\partial\hat{b}}{\partial x}\right), \quad (\text{B25})$$

771 and

$$\sigma\hat{b} = -\frac{\partial}{\partial x}\left(Q_b\hat{b} - Q_h\frac{\partial\hat{h}}{\partial x}\right) - K\kappa^2\hat{h} + \frac{M_b}{\rho_w}\hat{b} - \frac{U}{\rho_w}\hat{h} - \frac{M_h}{\rho_w}\frac{\partial\hat{h}}{\partial x} - \frac{\bar{m}\bar{b}}{\rho_w}\kappa^2\hat{b} + \frac{\partial}{\partial x}\left(\frac{\bar{m}\bar{b}}{\rho_w}\frac{\partial\hat{b}}{\partial x}\right). \quad (\text{B26})$$

772 This is once again an eigenvalue problem to find the growth rate σ corresponding to \hat{h}
 773 and \hat{b} which can only be solved numerically in general (figure 5).

774 However, if we anticipate only a small change from our previous analysis, we can
 775 go through the same simplifications and once again look primarily at the large κ (small
 776 wavelength) case, taking the same limit of small pressure variations, $\hat{h} \ll 1$, and chan-
 777 nels confined close to the terminus, $1/\kappa \ll x \ll 1$. Under these assumptions, equa-
 778 tions (B25-B26) reduce to

$$\left(\sigma - \frac{M_b}{\rho_i} + A\bar{N}^n + \frac{u_b}{l_r} + \frac{\bar{m}\bar{b}}{\rho_i}\kappa^2\right)\hat{b} = -\frac{M_h}{\rho_i}\frac{\partial\hat{h}}{\partial x}, \quad (\text{B27})$$

779 and

$$K\kappa^2\hat{h} = -Q_b\frac{\partial\hat{b}}{\partial x}. \quad (\text{B28})$$

780 These are structurally identical to the previous large κ limit, but with an additional $\bar{m}\bar{b}\kappa^2/\rho_i$
 781 multiplying \hat{b} in (B27). This means σ_D , the growth rate when $\hat{h} = 0$, is now

$$\sigma_D = \frac{M_b}{\rho_i} - A\bar{N}^n - \frac{u_b}{l_r} - \frac{\bar{m}\bar{b}}{\rho_i}\kappa^2 = \sigma_0(x_t) - \frac{\bar{m}\bar{b}}{\rho_i}\kappa^2 \quad (\text{B29})$$

782 and becomes stable as κ gets large.

783 B3 The case of cold ice

784 Throughout this paper, we have assumed the ice to be at melting point, neglect-
 785 ing heat fluxes into the ice. However, if there is a temperature gradient through the ice,
 786 tending towards a cold surface temperature, we should modify the balance of heat fluxes
 787 at the melting interface to include this loss toward the surface,

$$\dot{m}L = -k_w\frac{\partial T_w}{\partial n} + k_i\frac{\partial T_i}{\partial n}, \quad (\text{B30})$$

788 where k_w is the thermal conductivity of water and k_i is that of ice.

789 The analysis of heat fluxes in the water layer proceeds exactly as in section 3.3. In
 790 the ice, $T_i = \bar{T}_i + \hat{T}_i e^{i\kappa y}$ solves the heat equation with no heat source term, and, given
 791 the flow speed of ice, no advection term, so

$$\frac{d^2\hat{T}_i}{dz^2} - \kappa^2\hat{T}_i = 0. \quad (\text{B31})$$

792 Assuming that the ice is much deeper than the wavelength of the perturbations, tem-
 793 perature fluctuations decay towards the surface. Thus, the solution to (B31) with $T_i(b) =$
 794 T_m is given by

$$\hat{T}_i = -\frac{d\bar{T}_i}{dz}\hat{b}e^{-\kappa(z-b)} \quad (\text{B32})$$

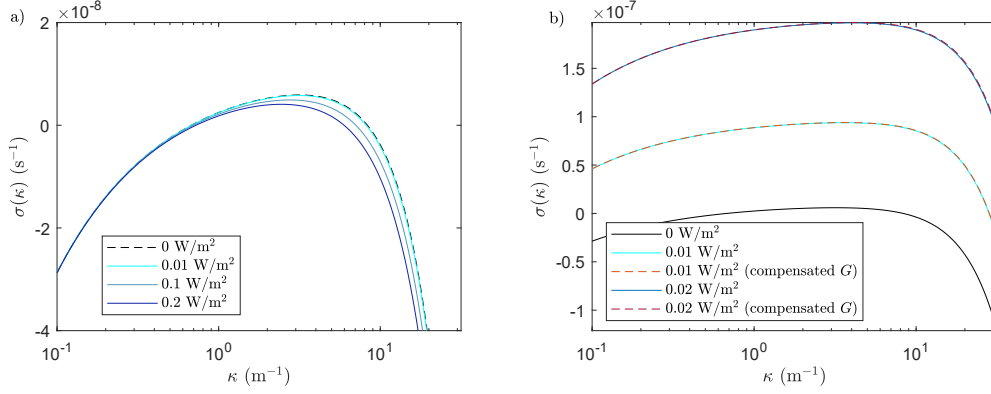


Figure B1. Impact of including a heat flux into the ice on the growth rate of perturbations, as given by (B35). a) Increasing G to compensate, so that the background state remains the same. This isolates the stabilising impact of lateral heat flux within the ice, which is minimal for realistic temperature gradients. b) Keeping G fixed, and thus with a lower net background heat flux. Dashed lines show equivalent curves for appropriately reduced G and temperate ice, indicating that altering G accounts for the majority of the change in dynamics.

795 and the perturbed heat flux into the ice is

$$k_i \frac{\partial \hat{T}_i}{\partial z} = k_i \frac{d\bar{T}_i}{dz} \kappa \hat{b}. \quad (\text{B33})$$

796 Inserting (B33) into (B30) we obtain, in the notation of (B24)

$$\hat{m} = \hat{m}_0 - \kappa^2 \bar{b} \bar{m} \hat{b} + \frac{k_i}{L} \frac{d\bar{T}_i}{dz} \kappa \hat{b}. \quad (\text{B34})$$

797 Note that the temperature gradient through the ice is negative, so this additional term
798 also stabilises the short wavelengths, representing the stabilising effects of lateral heat
799 flux through the ice as well as through the water.

800 Thus, the analytic expression for the growth rate of perturbations in the case of
801 cold ice is, by comparison with (45),

$$\sigma = \sigma_0(x_t) - \frac{\bar{m} \bar{b}}{\rho_i} \kappa^2 - \frac{k_i}{\rho_i L} \left| \frac{d\bar{T}_i}{dz} \right| \kappa - \Sigma \left(\frac{\partial \sigma_0}{\partial x} \right)^{2/3} \left(\frac{Q_b M_h}{\rho_i K \kappa^2} \right)^{1/3}. \quad (\text{B35})$$

802 Note that the background state also changes due to the reduction in melt-rate, since
803 heat is lost into the ice, so

$$\bar{m} = \frac{1}{L} \left(G - k_i \left| \frac{d\bar{T}_i}{dz} \right| + |\mathbf{u}_b \cdot \boldsymbol{\tau}_b| - \rho_w g \bar{q} \frac{d\bar{h}}{dx} \right). \quad (\text{B36})$$

804 Structurally this acts like a reduction in G and can be incorporated into the stability cri-
805 terion in this way.

806 Plots of the growth rate (B35) for a range of temperature gradients are shown in
807 figure B1. Figure B1a) shows that if the net background heat flux, $G - k_i |d\bar{T}_i/dz|$, is
808 unchanged, then the stabilising impact of lateral heat flux through the ice has minimal
809 impact on the growth rates of perturbations for realistic values of the ice temperature
810 gradient. However, figure B1b) shows that if G is kept fixed, the reduction in net back-
811 ground heat flux affects the growth rate much more dramatically, simply because decreas-
812 ing the net background heat flux reduces the value of \bar{b} , which increases σ_0 . For com-
813 parison, just changing the value of G without including heat fluxes through the ice yields
814 extremely similar results.

815 We therefore suggest that vertical temperature gradients within the ice should be
 816 accounted for via a reduction in G , but lateral temperature gradients have very little im-
 817 pact on the evolution of the subglacial hydrology and can be ignored in modeling.

818 **B4 Strongly varying ice thickness**

819 Our analysis has assumed that the maximum value of $\sigma_0(x)$ is always found at the
 820 terminus. This is true in our numerical examples, when the effective pressure tends to
 821 increase towards the terminus. However, if there is a very strong gradient in ice over-
 822 burdened pressure, the maximum growth rate can occur slightly inland. We jump to the
 823 large κ limit to see how this modifies the analytical growth rates.

824 In this case, perturbations are expected to occur localised around this maximum
 825 at $x = x_{max}$, rather than around the terminus. The relevant leading order expansion
 826 for $\sigma - \sigma_0(x)$ is now a quadratic,

$$\sigma_0(x) \approx \sigma_0(x_{max}) + \frac{1}{2} \frac{d^2\sigma_0}{dx^2} (x - x_{max})^2, \quad (\text{B37})$$

827 and we approximate all other functions of x by their values at x_{max} (rather than their
 828 values at the terminus).

829 Substituting this altered shape of the growth rate, the perturbed kinematic con-
 830 dition is

$$\left(\sigma - \sigma_0(x_{max}) - \frac{1}{2} \frac{d^2\sigma_0}{dx^2} (x - x_{max})^2 \right) \hat{b} = -\frac{M_h}{\rho_i} \frac{\partial \hat{h}}{\partial x} \quad (\text{B38})$$

831 while the perturbed conservation of mass is unchanged except in where Q_b and K are
 832 evaluated,

$$Q_b \frac{\partial \hat{b}}{\partial x} = -K \kappa^2 \hat{h}. \quad (\text{B39})$$

833 Combining these, we have

$$\frac{\partial^2 \hat{b}}{\partial x^2} = -\frac{K \kappa^2}{Q_b} \frac{\partial \hat{h}}{\partial x} = \frac{\rho_i K \kappa^2}{Q_b M_h} \left(\sigma - \sigma_0(x_{max}) - \frac{1}{2} \frac{d^2\sigma_0}{dx^2} (x - x_{max})^2 \right) \hat{b}. \quad (\text{B40})$$

834 To make progress, we now rescale with

$$\sigma(\kappa) - \sigma_0(x_{max}) = a \sqrt{\frac{2 \left| \frac{d^2\sigma_0}{dx^2} \right| Q_b M_h}{\rho_i K \kappa^2}}, \quad z = \left(\frac{2 \left| \frac{d^2\sigma_0}{dx^2} \right| \rho_i K \kappa^2}{Q_b M_h} \right)^{1/4} (x - x_{max}) \quad (\text{B41})$$

835 and obtain

$$\frac{\partial^2 \hat{b}}{\partial z^2} = \left(a + \frac{z^2}{4} \right) \hat{b}. \quad (\text{B42})$$

836 We look for values of a that permit a solution that decays as $z \rightarrow \pm\infty$, so as to fit both
 837 the upstream boundary condition (decay of the perturbation towards the ice divide, $z \rightarrow$
 838 $-\infty$) and downstream (imposed pressure head at the margin requiring decay as $z \rightarrow$
 839 ∞).

840 A symmetrically decaying solution to (B42) is possible whenever

$$\sin \left(\left(\frac{a}{2} + \frac{1}{4} \right) \pi \right) \Gamma \left(\frac{3}{4} - \frac{a}{2} \right) = 0, \quad (\text{B43})$$

841 but we want the maximum possible value of a , associated with the largest growth rate.
 842 This turns out to be $a = -1/2$, so

$$\sigma(\kappa) = \sigma_0(x_{max}) - \sqrt{\frac{\left| \frac{d^2\sigma_0}{dx^2} \right| Q_b M_h}{2 \rho_i K \kappa^2}}, \quad (\text{B44})$$

843 and the growth rate at large wavelengths now decays like $1/\kappa$. The associated shape of
844 the gap height perturbation

$$\hat{b} = \exp \left(- \left(\frac{2 \left| \frac{d^2 \sigma_0}{dx^2} \right| \rho_i K \kappa^2}{Q_b M_h} \right)^{1/2} \frac{(x - x_{max})^2}{4} \right) \quad (\text{B45})$$

845 is Gaussian function peaked around $x = x_{max}$

846 Open Research Section

847 Code for calculating the laterally uniform profiles, eigenfunctions, and growth rates,
848 is available on Zenodo (Warburton, 2024). Basilisk (Popinet, 2013–2024) now includes
849 the Basilisk implementation of SHAKTI. Simulations with the original implementation
850 of SHAKTI (Sommers et al., 2018) were done in ISSM Version 4.21 (Larour et al., 2012).
851 MEaSURES velocity data (Joughin et al., 2018) is available from Joughin et al. (2016).
852 We used BedMachine Version 4 (Morlighem et al., 2017).

853 Acknowledgments

854 KLPW was funded by the Dartmouth Society of Fellows; CRM acknowledges funding
855 from NSF (2012958), NASA (EPSCoR-80NSSC21M0329), the Army Research Office (78811EG),
856 and the Heising-Simons Foundation (2020–1911); and ANS was supported by the Heising-
857 Simons Foundation (2020–1911). We thank Mathieu Morlighem for support in sharing
858 the domain outline containing Russell Glacier and Isunnguata Sermia, and Lauren An-
859 drews for helpful discussion. Our thanks to the editor and three anonymous reviewers
860 for their time and helpful suggestions in improving this manuscript.

861 References

- 862 Andrews, L. C., Catania, G. A., Hoffman, M. J., Gulley, J. D., Lüthi, M. P., Ryser,
863 C., ... Neumann, T. A. (2014, Oct 01). Direct observations of evolving sub-
864 glacial drainage beneath the Greenland Ice Sheet. *Nature*, *514* (7520), 80–83.
865 doi: 10.1038/nature13796
- 866 Aschwanden, A., Fahnestock, M. A., Truffer, M., Brinkerhoff, D. J., Hock, R.,
867 Khroulev, C., ... Khan, S. A. (2019). Contribution of the Greenland Ice
868 Sheet to sea level over the next millennium. *Science advances*, *5*(6), eaav9396.
- 869 Bartholomew, I., Nienow, P., Sole, A., Mair, D., Cowton, T., Palmer, S., & Wad-
870 ham, J. (2011). Supraglacial forcing of subglacial drainage in the ablation
871 zone of the Greenland ice sheet. *Geophysical Research Letters*, *38*(8). doi:
872 https://doi.org/10.1029/2011GL047063
- 873 Benn, D. I., Fowler, A. C., Hewitt, I., & Sevestre, H. (2019). A general theory of
874 glacier surges. *Journal of Glaciology*, *65*(253), 701–716. doi: 10.1017/jog.2019
875 .62
- 876 Brinkerhoff, D. J., Aschwanden, A., & Fahnestock, M. (2021). Constraining
877 subglacial processes from surface velocity observations using surrogate-
878 based bayesian inference. *Journal of Glaciology*, *67*(263), 385–403. doi:
879 10.1017/jog.2020.112
- 880 Brinkerhoff, D. J., Meyer, C. R., Bueler, E., Truffer, M., & Bartholomew, T. C.
881 (2016). Inversion of a glacier hydrology model. *Annals of Glaciology*, *57*(72),
882 84–95. doi: 10.1017/aog.2016.3
- 883 Cornford, S. L., Martin, D. F., Lee, V., Payne, A. J., & Ng, E. G. (2016). Adaptive
884 mesh refinement versus subgrid friction interpolation in simulations of Antarc-
885 tic ice dynamics. *Annals of Glaciology*, *57*(73), 1–9. doi: 10.1017/aog.2016.13
- 886 de Fleurian, B., Werder, M. A., Beyer, S., Brinkerhoff, D. J., Delaney, L., Dow,
887 C. F., ... et al. (2018). SHMIP The subglacial hydrology model in-

- 888 tercomparison Project. *Journal of Glaciology*, 64(248), 897–916. doi:
889 10.1017/jog.2018.78
- 890 Dow, C. F. (2022). The role of subglacial hydrology in antarctic ice sheet dynamics
891 and stability: a modelling perspective. *Annals of Glaciology*, 63(87–89), 49–54.
892 doi: 10.1017/aog.2023.9
- 893 Felden, A. M., Martin, D. F., & Ng, E. G. (2023). SUHMO: an adaptive mesh re-
894 finement subglacial hydrology model v1.0. *Geoscientific Model Development*,
895 16(1), 407–425. doi: 10.5194/gmd-16-407-2023
- 896 Flowers, G. E. (2015). Modelling water flow under glaciers and ice sheets. *Proceed-*
897 *ings of the Royal Society A: Mathematical, Physical and Engineering Sciences*,
898 471(2176), 20140907.
- 899 Hager, A. O., Hoffman, M. J., Price, S. F., & Schroeder, D. M. (2022). Persist-
900 ent, extensive channelized drainage modeled beneath Thwaites Glacier, West
901 Antarctica. *The Cryosphere*, 16(9), 3575–3599. doi: 10.5194/tc-16-3575-2022
- 902 Helanow, C., Iverson, N. R., Woodard, J. B., & Zoet, L. K. (2021). A slip law for
903 hard-bedded glaciers derived from observed bed topography. *Science Advances*,
904 7(20), eabe7798. doi: 10.1126/sciadv.abe7798
- 905 Hewitt, D. R., Chini, G. P., & Neufeld, J. A. (2018). The influence of a poroelas-
906 tic till on rapid subglacial flooding and cavity formation. *Journal of Fluid Me-*
907 *chanics*, 855, 1170–1207. doi: 10.1017/jfm.2018.624
- 908 Hewitt, I. J. (2009). *Mathematical modelling of geophysical melt drainage* (PhD the-
909 sis). University of Oxford.
- 910 Hewitt, I. J. (2011). Modelling distributed and channelized subglacial drainage: the
911 spacing of channels. *Journal of Glaciology*, 57(202), 302–314. doi: 10.3189/
912 002214311796405951
- 913 Hewitt, I. J. (2013). Seasonal changes in ice sheet motion due to melt water lubri-
914 cation. *Earth and Planetary Science Letters*, 371–372, 16–25. doi: [https://doi](https://doi.org/10.1016/j.epsl.2013.04.022)
915 [.org/10.1016/j.epsl.2013.04.022](https://doi.org/10.1016/j.epsl.2013.04.022)
- 916 Hiester, J., Sergienko, O. V., & Hulbe, C. L. (2016). Topographically mediated ice
917 stream subglacial drainage networks. *Journal of Geophysical Research: Earth*
918 *Surface*, 121(2), 497–510. Retrieved from [https://agupubs.onlinelibrary](https://agupubs.onlinelibrary.wiley.com/doi/abs/10.1002/2015JF003660)
919 [.wiley.com/doi/abs/10.1002/2015JF003660](https://doi.org/10.1002/2015JF003660) doi: [https://doi.org/10.1002/](https://doi.org/10.1002/2015JF003660)
920 [2015JF003660](https://doi.org/10.1002/2015JF003660)
- 921 Hill, T., Flowers, G. E., Hoffman, M. J., Bingham, D., & Werder, M. A. (2023).
922 Improved representation of laminar and turbulent sheet flow in subglacial
923 drainage models. *Journal of Glaciology*, 1–14. doi: 10.1017/jog.2023.103
- 924 Joughin, I., Smith, B., Howat, I., & Scambos, T. (2016). *Measures*
925 *multi-year greenland ice sheet velocity mosaic (nsidc-0670, version 1)*.
926 <https://doi.org/10.5067/QUA5Q9SVMSJG> [Data Set].
- 927 Joughin, I., Smith, B. E., & Howat, I. M. (2018). A complete map of greenland ice
928 velocity derived from satellite data collected over 20 years. *Journal of Glaciol-*
929 *ogy*, 64(243), 1–11. doi: 10.1017/jog.2017.73
- 930 Kyrke-Smith, T. M., Katz, R. F., & Fowler, A. C. (2014). Subglacial hydrology and
931 the formation of ice streams. *Proceedings of the Royal Society A: Mathemat-*
932 *ical, Physical and Engineering Sciences*, 470(2161), 20130494. doi: 10.1098/
933 rspa.2013.0494
- 934 Larour, E., Seroussi, H., Morlighem, M., & Rignot, E. (2012). Continental scale,
935 high order, high spatial resolution, ice sheet modeling using the ice sheet sys-
936 tem model (issm). *Journal of Geophysical Research: Earth Surface*, 117(F1).
937 Retrieved from [https://agupubs.onlinelibrary.wiley.com/doi/abs/](https://agupubs.onlinelibrary.wiley.com/doi/abs/10.1029/2011JF002140)
938 [10.1029/2011JF002140](https://doi.org/10.1029/2011JF002140) doi: <https://doi.org/10.1029/2011JF002140>
- 939 MacGregor, J. A., Fahnestock, M. A., Catania, G. A., Aschwanden, A., Clow, G. D.,
940 Colgan, W. T., . . . Seroussi, H. (2016). A synthesis of the basal thermal state
941 of the Greenland Ice Sheet. *Journal of Geophysical Research: Earth Surface*,
942 121(7), 1328–1350. doi: <https://doi.org/10.1002/2015JF003803>

- 943 Maier, N., Humphrey, N., Harper, J., & Meierbachtol, T. (2019). Sliding dominates
 944 slow-flowing margin regions, Greenland Ice Sheet. *Science Advances*, *5*(7),
 945 eaaw5406. doi: 10.1126/sciadv.aaw5406
- 946 Moon, T., Joughin, I., Smith, B., van den Broeke, M. R., van de Berg, W. J.,
 947 Noël, B., & Usher, M. (2014). Distinct patterns of seasonal Greenland
 948 glacier velocity. *Geophysical Research Letters*, *41*(20), 7209–7216. doi:
 949 <https://doi.org/10.1002/2014GL061836>
- 950 Morlighem, M., Rignot, E., Seroussi, H., Larour, E., Ben Dhia, H., & Aubry, D.
 951 (2010). Spatial patterns of basal drag inferred using control methods from a
 952 full-stokes and simpler models for pine island glacier, west antarctica. *Geophys-*
 953 *ical Research Letters*, *37*(14). doi: <https://doi.org/10.1029/2010GL043853>
- 954 Morlighem, M., Williams, C. N., Rignot, E., An, L., Arndt, J. E., Bamber, J. L., ...
 955 Zinglensen, K. B. (2017). Bedmachine v3: Complete bed topography and ocean
 956 bathymetry mapping of greenland from multibeam echo sounding combined
 957 with mass conservation. *Geophysical Research Letters*, *44*(21), 11,051–11,061.
 958 doi: <https://doi.org/10.1002/2017GL074954>
- 959 Mouginot, J., Rignot, E., Bjørk, A. A., Van den Broeke, M., Millan, R., Morlighem,
 960 M., ... Wood, M. (2019). Forty-six years of Greenland Ice Sheet mass balance
 961 from 1972 to 2018. *Proceedings of the national academy of sciences*, *116*(19),
 962 9239–9244.
- 963 Nienow, P. W., Sole, A. J., Slater, D. A., & Cowton, T. R. (2017, Dec 01). Recent
 964 Advances in Our Understanding of the Role of Meltwater in the Greenland
 965 Ice Sheet System. *Current Climate Change Reports*, *3*(4), 330–344. doi:
 966 [10.1007/s40641-017-0083-9](https://doi.org/10.1007/s40641-017-0083-9)
- 967 Ootosaka, I., Shepherd, A., Ivins, E., Schlegel, N., Amory, C., van den Broeke, M., ...
 968 others (2023). *Mass balance of the Greenland and Antarctic ice sheets from*
 969 *1992 to 2020. Earth Syst Sci Data 15 (4): 1597-1616.*
- 970 Poinar, K. (2023). Seasonal flow types of glaciers in sermilik fjord, greenland,
 971 over 2016–2021. *Journal of Geophysical Research: Earth Surface*, *128*(7),
 972 e2022JF006901. doi: <https://doi.org/10.1029/2022JF006901>
- 973 Poinar, K., Dow, C. F., & Andrews, L. C. (2019). Long-Term Support of an Ac-
 974 tive Subglacial Hydrologic System in Southeast Greenland by Firn Aquifers.
 975 *Geophysical Research Letters*, *46*(9), 4772–4781. doi: [https://doi.org/10.1029/](https://doi.org/10.1029/2019GL082786)
 976 [2019GL082786](https://doi.org/10.1029/2019GL082786)
- 977 Popinet, S. (2013–2024). *Basilisk*. <http://basilisk.fr> [Software].
- 978 Rada, C., & Schoof, C. (2018). Channelized, distributed, and disconnected: sub-
 979 glacial drainage under a valley glacier in the Yukon. *The Cryosphere*, *12*(8),
 980 2609–2636. doi: 10.5194/tc-12-2609-2018
- 981 Rignot, E., & Mouginot, J. (2012). Ice flow in Greenland for the International Polar
 982 Year 2008–2009. *Geophysical Research Letters*, *39*(11). doi: [https://doi.org/10](https://doi.org/10.1029/2012GL051634)
 983 [.1029/2012GL051634](https://doi.org/10.1029/2012GL051634)
- 984 Schoof, C. (2005). The effect of cavitation on glacier sliding. *Proceedings of the*
 985 *Royal Society A: Mathematical, Physical and Engineering Sciences*, *461*(2055),
 986 609–627. doi: 10.1098/rspa.2004.1350
- 987 Schoof, C. (2010). Ice-sheet acceleration driven by melt supply variability. *Nature*,
 988 *468*(7325), 803–806. doi: 10.1038/nature09618
- 989 Schoof, C. (2023). The evolution of isolated cavities and hydraulic connection at
 990 the glacier bed. Part 1: steady states and friction laws. *EGUsphere*, *2023*, 1–
 991 27. doi: 10.5194/egusphere-2022-1380
- 992 Schoof, C., Hewitt, I. J., & Werder, M. A. (2012). Flotation and free surface flow in
 993 a model for subglacial drainage. part 1. distributed drainage. *Journal of Fluid*
 994 *Mechanics*, *702*, 126–156. doi: 10.1017/jfm.2012.165
- 995 Seroussi, H., Morlighem, M., Rignot, E., Khazendar, A., Larour, E., & Mouginot,
 996 J. (2013). Dependence of century-scale projections of the greenland ice
 997 sheet on its thermal regime. *Journal of Glaciology*, *59*(218), 1024–1034. doi:

- 10.3189/2013JoG13J054
- 998 Shapero, D. R., Joughin, I. R., Poinar, K., Morlighem, M., & Gillet-Chaulet, F.
999 (2016). Basal resistance for three of the largest greenland outlet glaciers.
1000 *Journal of Geophysical Research: Earth Surface*, *121*(1), 168–180. doi:
1001 <https://doi.org/10.1002/2015JF003643>
- 1002 Sommers, A., Meyer, C., Morlighem, M., Rajaram, H., Poinar, K., Chu, W., &
1003 Mejia, J. (2023). Subglacial hydrology modeling predicts high winter water
1004 pressure and spatially variable transmissivity at Helheim Glacier, Greenland.
1005 *Journal of Glaciology*, 1–13. doi: 10.1017/jog.2023.39
- 1006 Sommers, A., Rajaram, H., & Morlighem, M. (2018). SHAKTI: subglacial hydrology
1007 and kinetic, transient interactions v1.0. *Geoscientific Model Development*,
1008 *11*(7), 2955–2974. doi: 10.5194/gmd-11-2955-2018
- 1009 Tedstone, A. J., Nienow, P. W., Gourmelen, N., Dehecq, A., Goldberg, D., &
1010 Hanna, E. (2015, Oct 01). Decadal slowdown of a land-terminating sector
1011 of the greenland ice sheet despite warming. *Nature*, *526*(7575), 692–
1012 695. Retrieved from <https://doi.org/10.1038/nature15722> doi:
1013 10.1038/nature15722
- 1014 Vijay, S., King, M. D., Howat, I. M., Solgaard, A. M., Khan, S. A., & Noël, B.
1015 (2021). Greenland ice-sheet wide glacier classification based on two distinct
1016 seasonal ice velocity behaviors. *Journal of Glaciology*, *67*(266), 1241–1248. doi:
1017 10.1017/jog.2021.89
- 1018 Walder, J. S. (1982). Stability of sheet flow of water beneath temperate glaciers and
1019 implications for glacier surging. *Journal of Glaciology*, *28*(99), 273–293.
- 1020 Warburton, K. L. P. (2024). *kasiawarburton/shaktistability*.
1021 <https://zenodo.org/doi/10.5281/zenodo.10887090> [Software].
- 1022 Warburton, K. L. P., Hewitt, D. R., & Neufeld, J. A. (2023). Shear dilation of sub-
1023 glacial till results in time-dependent sliding laws. *Proceedings of the Royal*
1024 *Society A: Mathematical, Physical and Engineering Sciences*, *479*(2269),
1025 20220536. doi: 10.1098/rspa.2022.0536
- 1026 Werder, M. A., Hewitt, I. J., Schoof, C. G., & Flowers, G. E. (2013). Modeling chan-
1027 nelized and distributed subglacial drainage in two dimensions. *Journal of Geo-*
1028 *physical Research: Earth Surface*, *118*(4), 2140–2158. doi: [https://doi.org/10](https://doi.org/10.1002/jgrf.20146)
1029 [.1002/jgrf.20146](https://doi.org/10.1002/jgrf.20146)
- 1030 Zimmerman, R. W., Al-Yaarubi, A., Pain, C. C., & Grattoni, C. A. (2004).
1031 Non-linear regimes of fluid flow in rock fractures. *International Journal*
1032 *of Rock Mechanics and Mining Sciences*, *41*, 163–169. (Proceedings of
1033 the ISRM SINOROCK 2004 Symposium) doi: [https://doi.org/10.1016/](https://doi.org/10.1016/j.ijrmms.2004.03.036)
1034 [j.ijrmms.2004.03.036](https://doi.org/10.1016/j.ijrmms.2004.03.036)
- 1035 Zoet, L. K., & Iverson, N. R. (2020). A slip law for glaciers on deformable beds. *Sci-*
1036 *ence*, *368*(6486), 76–78. Retrieved from [https://www.science.org/doi/abs/](https://www.science.org/doi/abs/10.1126/science.aaz1183)
1037 [10.1126/science.aaz1183](https://www.science.org/doi/abs/10.1126/science.aaz1183) doi: 10.1126/science.aaz1183
- 1038 Zwally, H. J., Abdalati, W., Herring, T., Larson, K., Saba, J., & Steffen, K. (2002).
1039 Surface Melt-Induced Acceleration of Greenland Ice-Sheet Flow. *Science*,
1040 *297*(5579), 218–222. doi: 10.1126/science.1072708
- 1041